

Identifying Three-Dimensional Radiative Patterns Associated with Early Tropical Cyclone Intensification

Frederick Iat-Hin Tam^{1,2}, Tom Beucler^{1,2}, James H. Ruppert Jr.³

¹Faculty of Geosciences and Environment, University of Lausanne, Switzerland

²Expertise Center for Climate Extremes, University of Lausanne, Switzerland

³School of Meteorology, University of Oklahoma, Norman, OK, USA

Key Points:

- We extract three-dimensional radiative heating patterns critical to tropical cyclogenesis from WRF simulations
- Our data-driven model pinpoints time periods where radiative heating has a dominant effect on early TC intensification
- Downshear longwave anomaly patterns are more relevant to the genesis of Haiyan than azimuthally uniform ones

arXiv:2401.09493v5 [physics.ao-ph] 12 Aug 2024

Abstract

Cloud radiative feedback impacts early tropical cyclone (TC) intensification, but limitations in existing diagnostic frameworks make them unsuitable for studying asymmetric or transient radiative heating. We propose a linear Variational Encoder-Decoder (VED) framework to learn the hidden relationship between radiative anomalies and the surface intensification of realistic simulated TCs. The uncertainty of the VED model identifies periods when radiation has more importance for intensification. A close examination of the radiative pattern extracted by the VED model from a 20-member ensemble simulation on Typhoon Haiyan shows that longwave forcing from inner core deep convection and shallow clouds downshear contribute to intensification, with deep convection in the downshear-left quadrant having the most impact overall on the intensification of that TC. Our work demonstrates that machine learning can aid the discovery of thermodynamic-kinematic relationships without relying on axisymmetric or deterministic assumptions, paving the way for the objective discovery of processes leading to TC intensification in realistic conditions.

Plain Language Summary

How clouds react to heating from the sun and Earth’s surface, called Cloud Radiative Feedback (CRF), greatly affects how quickly tropical cyclones intensify in their early stage. Traditional methods to isolate CRF have limitations. In this manuscript, we demonstrate that machine learning can be applied to this problem and allows us to isolate, quantify, and visualize CRF with better spatial details than what is possible with traditional methods. One of the many things our machine-learning model can do is identify times when CRF is important and times when other processes are more important. Applying our model to two historical tropical cyclones shows that CRF in certain regions close to the tropical cyclones’ centers are crucial for their early intensification. This helps us understand how these storms form in real-world conditions.

1 Introduction

Recent advances in numerical weather prediction (NWP) models brought substantial improvements to tropical cyclone (TC) track predictions (Landsea & Cangialosi, 2018). However, predicting TC intensity (DeMaria et al., 2014; Cangialosi et al., 2020) remains challenging. One of the most elusive aspects of TC strength evolution relates to the formation (‘genesis’) and early intensification of TCs, which involves multiscale interaction between ambient large-scale circulation and small-scale organized convective clusters (Narenpitak et al., 2020).

Radiative feedback has been shown to be one of the leading factors in the spontaneous self-aggregation of tropical oceanic convection in non-rotating simulations of radiative-convective equilibrium (RCE; C. Muller & Bony, 2015; Wing et al., 2017; Fan et al., 2021). Including background rotation in idealized RCE experiments results in self-aggregation that forms rotating, TC-like systems (Carstens & Wing, 2020). Recent observational and modeling studies reveal four radiative feedbacks that can potentially affect TC intensity: (1) longwave environmental destabilization (Melhauser & Zhang, 2014), (2) radial gradient in radiative heating between cloudy areas and cloudless surroundings (Gray & Jacobson, 1977; Nicholls, 2015; Smith et al., 2020), (3) trapping of longwave radiation by clouds (Bu et al., 2014; Ruppert et al., 2020), and (4) diurnal radiative forcing at TC cloud anvil (Melhauser & Zhang, 2014; Ruppert & O’Neill, 2019). Processes (2) and (3) are linked, whereby the local greenhouse trapping by clouds causes a radiative heating gradient relative to the cloudless surroundings. Although smaller in magnitude than latent heating, radiation significantly affects TC intensity by influencing the spatial distribution of convection (Dai et al., 2023). During the genesis phase, removing processes (2) and (3) delay TC formation by a factor of 2 to 3 (C. J. Muller & Romps, 2018; Rup-

pert et al., 2020; Smith et al., 2020; Rios-Berrios, 2020). Processes (2) and (3) contribute to early TC intensification through radiation-driven transverse circulations (Nicholls, 2015). These circulations sustain TC convection by moistening the inner core (Ruppert et al., 2020), enhancing mid-level circulations (Yang et al., 2022), and protecting against shear-related ventilation (Rios-Berrios, 2020).

The effect of radiation on TC evolution is usually examined through the column Moist Static Energy (MSE) variance budget (Wing et al., 2017; Wu et al., 2021) and axisymmetric balanced dynamics (Ruppert et al., 2020; Navarro et al., 2017). Thermal forcing from diabatic processes drives the TC out of thermal wind balance; the secondary circulation then restored the balanced state (Willoughby, 1979). The Sawyer-Eliassen Equation (SEQ; Pendergrass & Willoughby, 2009) can diagnose such secondary circulations. However, the SEQ has limitations because it requires the TC to be in a quasi-steady state. Transient thermal forcings are smoothed out to satisfy the quasi-steady state assumption, and the SEQ solutions are only available in a two-dimensional radius-height plane. The lack of azimuthal context makes the SEQ framework suboptimal to study TC genesis pathways under shear (R. F. Rogers et al., 2020; Nam & Bell, 2021), and the role of asymmetric convection in TC intensity changes (R. Rogers et al., 2013; Zagrodnik & Jiang, 2014; Xu et al., 2017).

To address this lack of spatial context, we use machine learning (ML) models to advance our understanding of how spatial patterns affect TC intensification (McGovern et al., 2019). Specifically, we identify three-dimensional radiative heating structures relevant to TC intensification. In an ML modeling framework, these structures can be found with post-hoc attribution methods. Applying Explainable Artificial intelligence (XAI) tools to ML algorithms led to the discovery of potential vorticity patterns favoring TC rapid intensification during trough-TC interaction (Fischer et al., 2019) and outgoing longwave radiation patterns enhancing the predictability of North Atlantic extratropical circulation (Mayer & Barnes, 2021). In contrast to the post-hoc explanation methods, recent studies (e.g., Barnes et al., 2022; Behrens et al., 2022) have leveraged specialized architectures akin to the Variational Encoder-Decoder architecture used in this study to find hidden structures in climate model outputs without using XAI tools, alleviating attribution uncertainty (Mamalakis et al., 2023).

Using complex ML models for scientific discovery poses notable challenges. First, these models are highly nonlinear and often not interpretable, which limits their trustworthiness. Second, complex ML models demand substantial data quantities for robust performance, which proves problematic when dealing with limited data samples. For example, we rely on limited model hindcasts in this work because finding the 3D radiative patterns relevant for genesis requires training on full 3D radiative heating structures - a variable not available in observations and reanalysis data. To address these challenges, we have developed a linear variational encoder-decoder (VED) model that fulfills the main traits of interpretable ML models: (i) simulatability, ensuring simplicity for comprehensibility, and (ii) decomposability, meaning that the model has meaningful inputs and parameters (Lipton, 2018; Marcinkevičs & Vogt, 2023).

This research investigates the potential of interpretable ML models to discover realistic radiative heating structures relevant to TC intensification from limited data. We offer physical insights on how these structures may contribute to early TC intensification. We will also show that we can use the uncertainties and bias in the model predictions to isolate the exact period where radiative feedback is most relevant to TC intensification.

2 Data

2.1 Convection-Permitting Hindcasts of Two Tropical Cyclones

We analyze a 20-member set of WRF Version 4.3.1 (Skamarock, 2008) ensemble hindcast simulations of Typhoon Haiyan (2013) and a small set of simulations of Hurricane Maria (2017), ran at a convective-permitting resolution (3 km). The same set of simulations for Maria in Ruppert et al. (2020) is analyzed to evaluate if ML models can learn the same physical conclusion in that paper - disabling Cloud Radiative Feedback (CRF) disrupts tropical cyclogenesis. This set of simulations includes one Control (CTRL) experiment and 4 “no-CRF” sensitivity simulations. “No-CRF” simulations are produced by running the CTRL restart files at different times, albeit setting all hydrometeor terms in the longwave and shortwave schemes to be zero. The CTRL simulation was initialized from GEFS analysis and integrated from September 14, 2017, 1200 UTC to September 20, 2017, 1200 UTC. Readers are referred to Ruppert et al. (2020) for more details regarding the setup of the Maria experiments.

We use the Haiyan ensemble simulations to analyze the role of CRF in realistic conditions, i.e., without the no-CRF experiments. These simulations are constructed by dynamically downscaling the National Center for Environmental Prediction’s Global Ensemble Forecast System (GEFS) ensemble member outputs. The primary source of variability in the ensemble comes from the interaction between convection and slight variability in the GEFS synoptic conditions. The Haiyan WRF simulations are integrated from November 1, 2013, 00 UTC to November 8, 2013, 00 UTC, with a two-nested, 15km-3km horizontal grid spacing fixed model domain. The inner domain is around 3600x2200 km in size. Radiation is treated with the Rapid Radiative Transfer Model for GCMs (RRTMG; Iacono et al., 2008), and microphysics is treated using the Thompson and Eidhammer scheme (Thompson & Eidhammer, 2014). Other model physics are configured identically to the Maria simulations. The model contains 55 stretched vertical levels and is topped at 10 hPa. These simulations are assigned integer labels from 0 to 19. All simulations produce outputs at an hourly interval; these outputs are post-processed into a TC-relative framework by tracking the local maxima in 700-hPa absolute vertical vorticity, spatially smoothed with a 1.5-degree boxcar filter, and temporally filtered with a 3-point Gaussian filter to remove noise.

For Haiyan, while we use all the data for training and evaluation, we keep the analysis tractable by focusing on two ensemble members: Member 2, which intensifies at a quicker rate, and Member 11, which intensifies at a slower rate.

2.2 Cross-validation strategy

Following best machine learning practices, we divide the data into training, validation, and test sets. Evaluating model skills on data unseen during training ensures good prediction skills for out-of-sample data. This section discusses how we perform the data splitting.

Since ensemble simulations and sensitivity experiments can be treated as different realizations of the same physical system responding to slightly different forcing, we opt for a data-splitting strategy based on ensemble member labels (Haiyan) and experiment labels (Maria).

For Haiyan, we use 80% of the ensemble outputs (16 experiments) for training, and 20% of the data (4 experiments) for validation and testing. Two experiments that are not strongly correlated to the other experiments are left out at first to create an independent test set; the remaining 18 experiments are partitioned into training and validation subsets by randomly generating a list of two numbers between 1 and 20; the two numbers are then used as references to separate the validation set from the training set.

This data-splitting procedure is repeated forty times to create forty different sets of training data, which enables evaluations of the model variability associated with the choice of data split. Our test set is truly independent because the two test experiments are never used in the training or validation set for all data splits.

We slightly altered the data-splitting strategy for Maria due to a lack of samples. The Control (CTRL) simulation is always included in the training set because it has the most samples and represents how the TC evolves in realistic conditions where CRF always exists. The “NCRF-36h” experiment is used as the test dataset amongst the four remaining sensitivity experiments because the storm intensity changes in that experiment depart most from the CTRL simulation. We randomly split the other experiments into a portion that is merged into the training set (2 experiments) and the other portion for model validation (1 experiment). The cross-validation strategy for Maria yields three different data splits to test the ability of the trained ML models to depict the counterfactual of TC evolution without cloud radiative feedback (CRF).

3 Methodology

3.1 Machine Learning Framework

Our analysis leverages machine learning (ML) to identify radiative spatial features relevant to TC intensification from WRF output. We adopt an interpretable, stochastic linear VED model to discover such features. Latent heating is not used as an input because it is treated as an internal response to external forcings such as radiation in the moist static energy variance budget (Wing & Emanuel, 2014; Wing, 2022). A schematic diagram of our framework is provided in Fig 1. The framework is divided into two parts: a learned encoder and a learned decoder for TC surface intensity predictions. The learned encoder distills radiative information relevant to TC intensity predictability into a limited number of structures. We constrain the number of extracted structures (one per variable in our case) to maximize interpretability and avoid model overfitting. The encoder incorporates Principal Component Analysis (PCA) to compress three-dimensional WRF longwave radiation and shortwave radiation outputs into multiple low-dimensional PCs, each representing the time evolution of a particular radiative anomaly pattern. The PCA reduces the complexity of the data from three-dimensional volumes to 1D time series. The encoder distills knowledge by combining the PCs into traceable compressed representations based on skillful TC intensity forecasts. The scalar output of the encoder is the projection of the radiation structures of individual samples onto the learned time-invariant structures, which roughly represents the spatial similarity between the two structures. We use these scalars to predict the 24-hour, forward-facing ($V_{t+24} - V_t$) intensification of TC surface intensity with a linear decoder. A lead time of 24 hours is commonly used for short-term intensity predictions (Law & Hobgood, 2007). All models presented herein are implemented and trained with the PyTorch deep learning library (Paszke et al., 2019). As shown in Section 3.2, the linear VED framework can be considered a combination of different multiple linear regression (MLR) equations. Training an ML model involves using an iterative procedure called “stochastic gradient descent” (SGD) to progressively optimize the weights and biases of the different MLR equations. The SGD procedure for all models is performed with the Adam Optimizer. Whether or not an ML model can reach an optimal solution depends on the “learning rate”, the step at which the SGD procedure proceeds, and a well-designed loss function. Loss functions are quantifiable measurements that are tied to the optimization process. An example of this is optimizing a model by minimizing a loss function like the mean squared error (MSE) between model predictions and observations. The VED architecture requires a specialized loss function for optimization. The VED architecture can be considered a generalized form of the Variational Autoencoder (VAE) architecture that uses different input-output pairs. Thus, the loss function used to optimize the VED model has the same structure as that commonly used for VAEs:

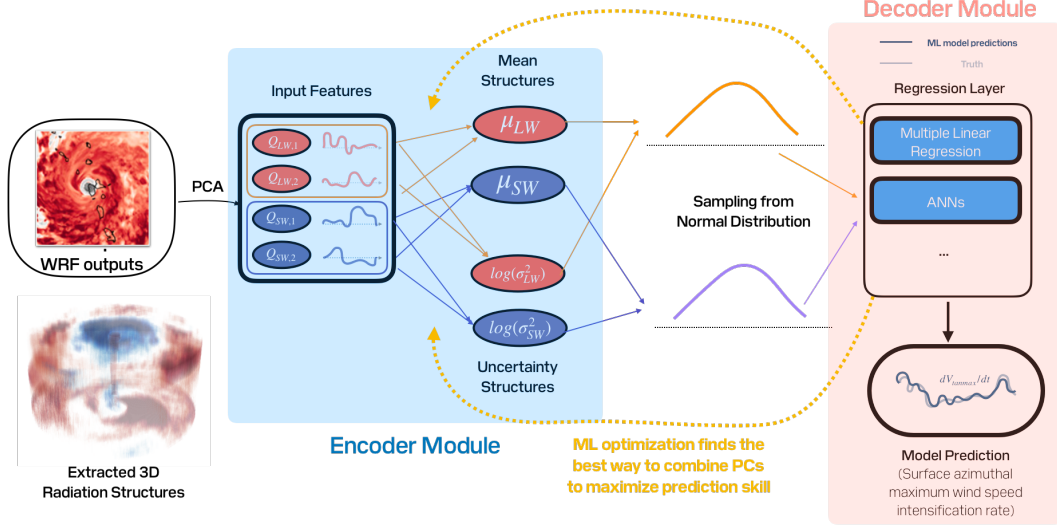


Figure 1. The interpretable linear VED framework proposed in this study combines a pattern-finding encoder and a decoder for TC intensification rate prediction. The first linear layer in the encoder modules combines different radiation structural information in the PCs into the time evolutions of the mean structures and uncertainty structures. A random sampling of the normal distributions with mean and log variances conditioned on the inputs introduces uncertainty to a decoder module that predicts the 24-hour surface wind intensification prediction. There is flexibility in the choice of the decoder architecture, from simple multiple linear regressors to a complex nonlinear Artificial Neural Network (ANN). Optimization of model weights with loss functions tries to minimize the absolute error between the truth and the predictions from the decoder based on the learned patterns.

$$\text{VEDloss} = \nu \text{Reconstruction Loss} + (1 - \nu) \text{KLloss}, \quad (1)$$

where $\nu \in [0, 1]$ is the weight of the reconstruction loss in the overall VED loss. The reconstruction loss measures how well the model predicts the output (a simple mean absolute error in our case), whereas the KL loss constrains the distribution of the latent space. We use an annealing strategy to train the VED models. The models are first optimized with only the reconstruction loss. We will then continue training the best model with the smallest reconstruction loss with different ν to optimize the prediction spread. The “learning rate” and ν are model hyperparameters - parameters that define the architecture of an ML model and its training. The best sets of hyperparameters for different data splits are found with the Optuna hyperparameter tuning framework (Akiba et al., 2019).

Various aspects of the proposed framework will be elaborated upon in this section. First, we demonstrate that the extracted patterns and their contributions to the VED predictions can be mathematically defined, ensuring full interpretability (Section 3.2). Second, we describe methods to incorporate uncertainty quantification in the framework (Section 3.3), which is critical in physical discovery (e.g., for Section 4.2). Finally, we present the metrics used in this work to evaluate prediction skills (Section 3.4).

3.2 Mathematical Construction of the Interpretable VED Models

As a whole, the main objective of the proposed VED model can be described by a simple equation:

$$\underbrace{\left(\frac{dV_{\text{surf}}}{dt}\right)_{24hr}}_{\text{Intensification}} = b + \underbrace{a_{\text{LW}} \cdot X_{\text{LW}}}_{\text{Longwave contribution}} + \underbrace{a_{\text{SW}} \cdot X_{\text{SW}}}_{\text{Shortwave contribution}} \quad (2)$$

where the prediction target is the temporal change in maximum tangential mean surface winds (V_{surf}) in units of m/s. Radiative contributions to the prediction are proportional to linear regression coefficients a_{LW} and a_{SW} (in units of $\text{m.s}^{-1}.\text{K}^{-1}$). The intercept term (b ; units in m/s^2) in the equation can be thought of as the intensification's expected value over the training set (positive in our case). Intensification rates predictions can be calculated from the sum of radiative contributions (X_{LW} , X_{SW}) that are sampled from normal distributions \mathcal{N} , with learned means (μ_{LW} , μ_{SW}) and learned logarithmic standard deviations ($\log\sigma_{\text{LW}}^2$, $\log\sigma_{\text{SW}}^2$):

$$X_{\text{LW}} \sim \mathcal{N}(\mu_{\text{LW}}, \log\sigma_{\text{LW}}^2) , \quad X_{\text{SW}} \sim \mathcal{N}(\mu_{\text{SW}}, \log\sigma_{\text{SW}}^2) \quad (3)$$

These four statistical moments are constructed with the learned weights and biases in the VED encoder module, and we will show that the conditional means μ_{LW} and μ_{SW} can be interpreted as projections of the longwave and shortwave fields onto data-driven, three-dimensional patterns. We will further show that the linear regression coefficient and intercept term can be defined with the learned weights and biases for both the encoder and decoder modules.

3.2.1 Encoder

As mentioned previously, Principal Component Analysis (PCA) extracts information from the WRF raw fields. The PCA linearly transforms input physical fields (X_i) into combinations of orthogonal singular (PCA) spatial modes ($\Pi_{X_i}(z, r, \theta)$), and their corresponding time evolution (PC loadings time series; $PC_{X_i}(t)$):

$$X_i(t, z, r, \theta) - \overline{X_i(t, z, r, \theta)} = \sum_{i=1}^N PC_{X_i}(t) \Pi_{X_i}(z, r, \theta), \quad (4)$$

where N is the number of retained PCA modes. Instead of the raw field, different loadings $PC_{X_i}(t)$, which represents the time evolution of different radiative spatial modes, are used as inputs to the VED. These $PC_{X_i}(t)$ time series are standardized to have a mean of 0 and a variance of 1 to avoid high variance in the regression weights:

$$\widetilde{PC}_{X_i}(t) = \frac{PC_{X_i}(t) - \overline{PC_{X_i}(t)}}{\sigma_{PC_{X_i}(t)}}, \quad (5)$$

where $\overline{PC_{X_i}}$ and $\sigma_{PC_{X_i}(t)}$ are the mean and standard deviation of the PC loadings, calculated over the training set.

The second task of the encoder is to combine different PCA modes for longwave radiation and shortwave radiation into two scalars representing the projection of radiation structures onto time-invariant “mean structures” ($\Pi_{\text{LW},\mu}$, $\Pi_{\text{SW},\mu}$) and two scalars representing the projection onto “logarithmic variance structures” ($\Pi_{\text{LW},\log\sigma^2}$, $\Pi_{\text{SW},\log\sigma^2}$). These four projection scalars (encoder output) are the linear combinations of the stan-

standardized PC loadings (Eq. 5),

$$\begin{aligned}
\mu_{LW} &= b_{1,LW,\mu} + \sum_{i=1}^{n_{LW}} a_{1,LW,\mu,i} \times \widetilde{PC}_{LW,i}, \\
\log \sigma_{LW}^2 &= b_{1,LW,\log \sigma^2} + \sum_{i=1}^{n_{LW}} a_{1,LW,\log \sigma^2,i} \times \widetilde{PC}_{LW,i}, \\
\mu_{SW} &= b_{1,SW,\mu} + \sum_{i=1}^{n_{SW}} a_{1,SW,\mu,i} \times \widetilde{PC}_{SW,i}, \\
\log \sigma_{SW}^2 &= b_{1,SW,\log \sigma^2} + \sum_{i=1}^{n_{SW}} a_{1,SW,\log \sigma^2,i} \times \widetilde{PC}_{SW,i}.
\end{aligned} \tag{6}$$

In these equations, terms with a and b represent the learned weights and biases in the VED framework, respectively. The subscripts in these terms have different options highlighting different aspects of the framework: “1” and “2” represent learned weights and biases in the encoder module and the decoder module; “LW” and “SW” represent the physical variables these coefficients are associated with (longwave and shortwave radiation). Finally, μ and $\log \sigma^2$ indicate the specific branch these coefficients are in within the VED framework (mean structure and uncertainty structure).

From Equation 2, the scalars defined in Equations 6 will be used to construct normal distributions $\mathcal{N}(\mu, \log \sigma^2)$ for longwave and shortwave radiation. Each time the VED model is run, two scalars will be randomly sampled from the two normal distributions and used as inputs in the prediction equation (Eq. 2). We could quantify the uncertainty of the prediction of TC intensification rates by running the model multiple times with the same inputs.

3.2.2 Interpreting the Encoding as a Scaled Projection

In addition to guiding how to combine the different PC modes, the learned encoder weights can also be used to obtain the 3-D spatial patterns corresponding to the four scalars (Eq. 6),

$$\begin{aligned}
\Pi_{\mu LW} &= \lambda_{LW,\mu} \sum_{i=1}^{n_{LW}} a_{1,LW,\mu,i} \times \Pi_{LW,i}, \\
\Pi_{\mu SW} &= \lambda_{SW,\mu} \sum_{i=1}^{n_{SW}} a_{1,SW,\mu,i} \times \Pi_{SW,i}, \\
\Pi_{\log \sigma^2 LW} &= \lambda_{LW,\log \sigma^2} \sum_{i=1}^{n_{LW}} a_{1,LW,\log \sigma^2,i} \times \Pi_{LW,i}, \\
\Pi_{\log \sigma^2 SW} &= \lambda_{SW,\log \sigma^2} \sum_{i=1}^{n_{SW}} a_{1,SW,\log \sigma^2,i} \times \Pi_{SW,i},
\end{aligned} \tag{7}$$

where λ represents scaling factors that ensure the extracted patterns have a norm of 1. The full mathematical deviation of this constant is shown in Appendix A.

But how are the scalars (Eqs. 6) and the spatial patterns (Eqs. 7) related? In this section, we show that the scalars are scaled projections of raw fields onto the time-invariant patterns. We first introduce an inner product that will help us reinterpret the encoder module:

$$\langle PC_{X_1} | PC_{X_2} \rangle_{X_3} = \sum_{i=1}^N PC_{X_1}^i PC_{X_2}^i, \tag{8}$$

where the X_3 subscript indicates that the inner product and the projection are defined with respect to the X_3 variable for which the PC decomposition and orthogonal modes

are calculated. Using this notation, the longwave conditional mean scalar (μ_{LW}) can be expressed as the projection of the spatiotemporal longwave heating field onto $\Pi_{\mu LW}$:

$$\underbrace{\mu_{LW}(t)}_{\text{Conditional Mean}} = \left\langle \underbrace{LW'(x, y, z, t)}_{\text{Longwave Heating Anomaly}} \mid \underbrace{\Pi_{LW, \mu}(x, y, z)}_{\text{Data-Driven Pattern}} \right\rangle_{LW}. \quad (9)$$

Indeed, the PC loadings ($PC_{i, \Pi_{\mu LW}}, PC_{i, \Pi_{\mu SW}}, PC_{i, \Pi_{\log \sigma^2 LW}}, PC_{i, \Pi_{\log \sigma^2 SW}}$) of the learned mean ($\Pi_{\mu LW}, \Pi_{\mu SW}$) and standard deviation ($\Pi_{\log \sigma^2 LW}, \Pi_{\log \sigma^2 SW}$) obey the following equations:

$$\begin{cases} \mu_{LW} = \langle LW' \mid \Pi_{\mu LW} \rangle_{LW} &= \sum_{i=1}^{n_{LW}} PC_{i, LW} \times PC_{i, \Pi_{\mu LW}}, \\ \log \sigma_{LW}^2 = \langle LW' \mid \Pi_{\log \sigma^2 LW} \rangle_{LW} &= \sum_{i=1}^{n_{LW}} PC_{i, LW} \times PC_{i, \Pi_{\log \sigma^2 LW}}, \\ \mu_{SW} = \langle SW' \mid \Pi_{\mu SW} \rangle_{SW} &= \sum_{i=1}^{n_{LW}} PC_{i, SW} \times PC_{i, \Pi_{\mu SW}}, \\ \log \sigma_{SW}^2 = \langle SW' \mid \Pi_{\log \sigma^2 SW} \rangle_{SW} &= \sum_{i=1}^{n_{LW}} PC_{i, LW} \times PC_{i, \Pi_{\log \sigma^2 SW}}, \end{cases} \quad (10)$$

allowing us to interpret the conditional moments ($\mu_{LW}, \mu_{SW}, \log \sigma_{LW}^2, \log \sigma_{SW}^2$) as projections of raw radiative heating fields onto stationary patterns. Using this projection notation, Equation 2 may be rewritten as:

$$\begin{aligned} \underbrace{\left(\frac{dV_{surf}}{dt} \right)_{24hr}}_{\text{Intensification}} &= \underbrace{a_{LW} \mathcal{N} \left(\langle LW \mid \Pi_{\mu LW} \rangle_{LW}, c_{LW} e^{d_{LW} \langle LW \mid \Pi_{\log \sigma_{LW}^2} \rangle_{LW}} \right)}_{\text{Longwave contribution}} \\ &+ \underbrace{a_{SW} \mathcal{N} \left(\langle SW \mid \Pi_{\mu SW} \rangle_{SW}, c_{SW} e^{d_{SW} \langle SW \mid \Pi_{\log \sigma_{SW}^2} \rangle_{SW}} \right)}_{\text{Shortwave contribution}} \\ &+ b, \end{aligned} \quad (11)$$

where the c_{LW} , c_{SW} , d_{LW} , and d_{SW} are constants involved when expanding the variance terms. The definitions of these terms are provided in the next section.

3.2.3 Effective Weights and Biases in the Prediction Equation

In this section, we will define several terms that are left undefined in previous sections. These undefined terms include the “effective weights” and bias terms in Equation 2, the scaling factor in Equation 6, and the four variance constants terms in Equation 11. The exact deviation steps for these terms can be found in Appendix A.

The “effective weights” terms can be obtained by factoring out the constant terms in the normal distributions after expanding Equation 2 with Eq. 5 and 6.

The effective weight of the longwave contribution to TC intensification is,

$$a_{LW} = |a_{2, LW}| \sqrt{\sum_{i=1}^{n_{LW}} \frac{a_{1, LW, \mu, i}^2}{\sigma (PC_{i, LW})^2}}, \quad (12)$$

whereas the effective weight of the shortwave contribution is

$$a_{SW} = |a_{2, SW}| \sqrt{\sum_{i=1}^{n_{SW}} \frac{a_{1, SW, \mu, i}^2}{\sigma (PC_{i, SW})^2}}. \quad (13)$$

The overall model bias (b), which can be thought of as the intensification’s expected value over the training set (positive in our case), can be obtained by substituting Equation 2 with Equations 5 and 6 and isolating constant terms that are not in the normal

distributions:

$$b = b_2 + a_{2,LW} \left(b_{1,LW,\mu} - \sum_{i=1}^{n_{LW}} \frac{a_{1,LW,\mu,i} \overline{PC_{i,LW}}}{\sigma(PC_{i,LW})} \right) + a_{2,SW} \left(b_{1,SW,\mu} - \sum_{i=1}^{n_{SW}} \frac{a_{1,SW,\mu,i} \overline{PC_{i,SW}}}{\sigma(PC_{i,SW})} \right). \quad (14)$$

This term will be referred to as “persistence baseline” in the subsequent sections. Physically, this term can be considered as the main contribution of non-radiative processes to the intensification of all training TCs.

The scaling factors for the four extracted patterns are mathematically derived by (i) combining equations 2, 6, and 5, (ii) building upon the equivalence of Equation 11 and the output equation from (i), and (iii) assuming the norms (squared) of the structures to be 1. For the mean longwave structure, the scaling factor is,

$$\lambda = \left[|a_{2,LW}| \sqrt{\sum_{i=1}^{n_{LW}} \frac{a_{1,LW,\mu,i}^2}{\sigma(PC_{i,LW})^2}} \right]^{-1}. \quad (15)$$

λ for the other scalars can be similarly defined by substituting the encoder weights and PC loading time series with those corresponding to the shortwave radiation and the logarithmic variance structures.

Finally, algebraic manipulations allow us to mathematically define the four constants involved in the variance calculation ($c_{LW}, c_{SW}, d_{LW}, d_{SW}$):

$$c_{LW} = \sqrt{\frac{|a_{2,LW}|}{a_{LW}}} \exp \left(b_{1,LW,\log \sigma^2} - \sum_{i=1}^{n_{LW}} a_{1,LW,\log \sigma^2,i} \frac{\overline{PC_{i,LW}}}{\sigma(PC_{i,LW})} \right), \quad (16)$$

$$c_{SW} = \sqrt{\frac{|a_{2,SW}|}{a_{SW}}} \exp \left(b_{1,SW,\log \sigma^2} - \sum_{i=1}^{n_{SW}} a_{1,SW,\log \sigma^2,i} \frac{\overline{PC_{i,SW}}}{\sigma(PC_{i,SW})} \right), \quad (17)$$

$$d_{LW} = \sqrt{\sum_{i=1}^{n_{LW}} \frac{a_{1,LW,\log \sigma^2,i}^2}{\sigma(PC_{i,LW})^2}}, \quad (18)$$

$$d_{SW} = \sqrt{\sum_{i=1}^{n_{SW}} \frac{a_{1,SW,\log \sigma^2,i}^2}{\sigma(PC_{i,SW})^2}}. \quad (19)$$

In the prediction equation, positive longwave contributions to surface wind intensification arise when the values sampled from $\mathcal{N}(\mu_{LW}, \sigma_{LW})$ are greater than zero. Positive longwave contributions will lead to intensification quicker than the training set reference (b), and vice versa. A quicker intensification occurs when the spatial distribution of longwave anomaly relative to the training average projects strongly onto $\Pi_{\mu_{LW}}$. In contrast, smaller intensification rates correspond to cases in which longwave anomalies and $\Pi_{LW,\mu}$ are orthogonal to each other. Similar logic can be applied to the shortwave contributions.

3.3 Uncertainty Quantifications for Physical Insights

By setting up a normal distribution based on the learned μ and $\log \sigma^2$ (Kingma & Welling, 2013), the proposed VED enables uncertainty quantification (UQ) for both the

extracted structures and the intensification predictions. This section touches upon how we may use VED uncertainty for physical insights.

The ML models are more trustworthy when they provide the full distribution of possible extracted structures and prediction outcomes. The full distributions yield uncertainty information that can be reliably interpreted, which is crucial when we use data-driven techniques to discover new physical processes. For example, we can use prediction uncertainties to assess the relevance of radiation with time. In contrast, uncertainties in the latent structures highlight specific areas in the structure to focus on in future work for scientific discovery.

One of the potential limitations in the current VED setup, especially when applying to the tropical cyclogenesis problem, is that we predict intensification with only the longwave and shortwave radiation information. It is likely that all pathways to tropical cyclone genesis and intensification are not included in this underdetermined system. We adopted this strategy because we are in a low sample regime, which necessitates restricting the input to avoid overfitting. However, the restricted nature of the model creatively yields physical understanding. Specifically, we argue that the temporal evolutions of model spread and error reveal the changes in the relevance of radiative feedback with time. Large spread and errors should arise when the system is undetermined and requires information from non-radiatively-coupled variables for reliable intensification predictions. These are periods where non-radiative processes are more important predictors of TC intensification. In contrast, we expect smaller model errors and spread when radiative heating is strongly coupled to intensification.

3.4 Evaluating the Trained Probabilistic Models

The trained VED models are evaluated with two criteria – good mean prediction skills and a well-calibrated uncertainty in the model outputs. We sample the model spread by running each model 30 times and aggregating the 30 model predictions. A suite of stochastic and determinative performance metrics are used to assess the quality of the model. Two stochastic metrics are evaluated: the Continuous Ranked Probability Score (CRPS score) and the Spread-skill reliability (SSREL) value (Haynes et al., 2023).

The CRPS score compares the Cumulative Distribution Function (CDF) of the probabilistic forecasts against the observations; it is also a generalization of the deterministic mean absolute error (MAE) metric for probabilistic models:

$$\text{CRPS}(F, y_{\text{true}}) = \int_{-\infty}^{\infty} [F(y_{\text{pred}}) - \mathcal{H}(y_{\text{pred}} - y_{\text{true}})]^2 dy_{\text{pred}}, \quad (20)$$

where F represents the CDF of the model predictions, \mathcal{H} is the Heaviside step function applied to the difference between the truth (y_{true}) and one prediction (y_{pred}) sampled from the full distribution. A well-calibrated model should have as small a CRPS score as possible.

The SSREL value (Haynes et al., 2023) measures the quality of a binned spread-skill plot – an assessment of the statistical consistency of a probabilistic model (Delle Monache et al., 2013). A statistically consistent model, sampled from the same distribution as the truth, should have its spread closely match its error. If the spread-skill curve of a model deviates from the 1-1 line, the model is either under-dispersive (overconfident) or over-dispersive (underconfident). The SSREL value measures weighted distances between the model curve and the 1-1 line:

$$\text{SSREL} = \sum_{k=1}^K \frac{N_k}{N} [\text{RMSE}_k - \overline{\text{SD}}_k], \quad (21)$$

where K is the number of bins, N_k is the number of samples in a bin, N is the total number of samples, RMSE_k is the root-mean-square-error of the model predictions for sam-

ples within the bin, SD is the standard deviation of the model predictions. A perfectly calibrated model will have an SSREL value of 0. We report two metrics for the mean deterministic skills: the mean absolute error (MAE) and root mean squared error (RMSE).

4 Results

An advantage of our proposed model architecture is that it simultaneously extracts structures relevant to 24-hour intensification rates and the uncertainties in the predictions. Here, we explore using this information to understand (i) how we can use ML to identify temporal periods where radiation is an important driver of intensification, (ii) the relevance of axisymmetric radiation to intensification, (iii) whether asymmetric radiation exerts influence on intensification, and (iv) whether we can show this influence with simple perturbation experiments.

4.1 Choosing the Best VED Model and Comparison with the Best Baseline Model

It is important to present evidence that the proposed VED model achieves better probabilistic skills than the traditional baseline. Here, we compare the best VED model to a simple Principal Component Regression baseline (description in Appendix B). The best VED model is chosen objectively based on the CRPS and SSREL scores. Figure 2 shows the minimum and median CRPS scores for all trained Haiyan VED and baseline models with different hyperparameters on the validation set. We also substitute the fully linear prediction layer in the baseline model with feed-forward neural networks with different depths to evaluate the responses of prediction skills to nonlinearity.

Adding nonlinearity degrades the median CRPS scores for most baseline models (Fig. 2a, c), which justifies keeping the model fully linear. The shape of the CRPS score curves for the baseline models (Fig. 2a, c) suggests the existence of an optimal range of **dropout rates** for better generalizability. For the VED models, a λ that is too small, i.e., too large a KL loss during training deteriorates prediction skills.

The CRPS score comparison above establishes optimal ranges for the **dropout rates** (the baseline models) and λ (the VED models). The best models for comparison are determined by calculating the SSREL scores for all models trained with these optimal coefficients. The spread-skill plot for the best baseline and VED models (Fig. 2) provides a strong justification for using the VED model in our study. Specifically, the spread-skill curve of the VED model is much shorter than the baseline one, which indicates the VED predictions are more accurate. Compared to the best baseline model, the best VED model better captures the peaks in the training dataset and removes the large biases in early intensification rates seen in the baseline predictions on the test set. Based on these comparisons, we conclude that the VED model is superior to the baseline model for our research task.

For Maria, the best VED model performs similarly to the best baseline model in terms of the minimum CRPS score (Fig. 2c). The uncertainty for both the best baseline model and best VED model are well calibrated. However, the VED model is again preferable for Maria because of the smaller prediction errors (Fig. 2d).

Interestingly, the benefit of the VED model compared to the baseline model seems to scale to the sample size. The VED model always overperforms the baseline for the Haiyan ensemble case with a larger sample size (Table 1), whereas the VED model mostly only overperforms the baseline in probabilistic metrics for the Maria simulations (Table 2). A potential explanation for worse VED skills for Maria is that the more complex model (VED) overfits the training data in cases with low sample size.

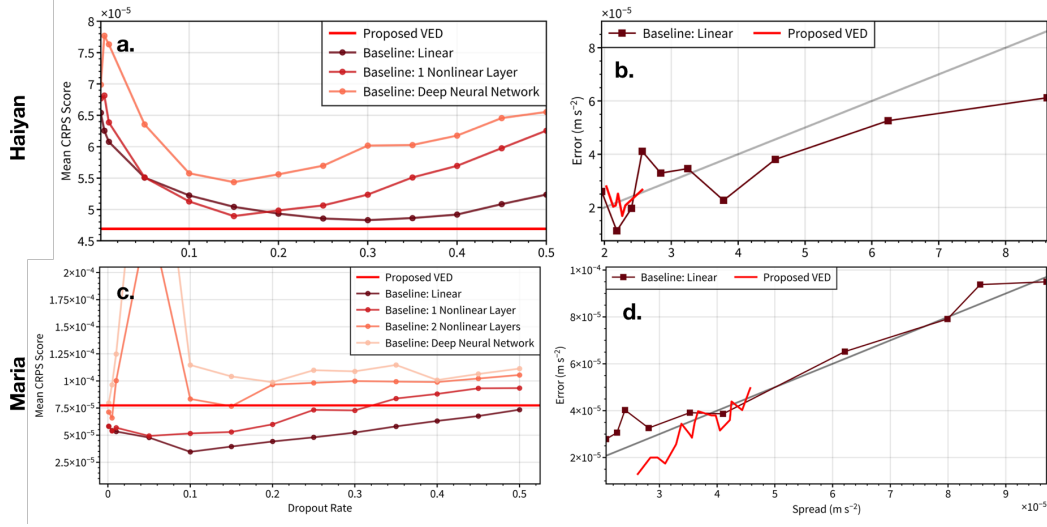


Figure 2. The mean CRPS scores (left column) and the spread-skill diagrams (right column) show that the trained VED models outperform the trained baseline models with different dropout rates and degrees of nonlinearity in the prediction equation (“nonln:3” represents baseline model with three nonlinear layers in the decoder). Comparing the best fully linear baseline model for Haiyan and Maria (brown lines in panel b and d; **dropout rates** of 0.3 and 0.1 respectively) and the mean performance of the VED model with the best SSREL score shows that the VED model makes fewer mistakes in its predictions and is generally more well-calibrated than the best baseline model. A well-calibrated model means that most points on the model’s spread-skill curve are as close to the 1-1 line (gray lines in b, d) as possible.

Table 1. Prediction skills of the best VED and the best baseline model on the Haiyan ensemble. Also shown in the table is the median of the prediction skills distribution of all trained models with different hyperparameter settings (numbers in brackets). All values in the table are multiplied by 10^5 for readability. The best model is indicated with bolded numbers.

| Experiment | Metric | Training | Validation | Test |
|------------|--------|--------------------|--------------------|--------------------|
| VED | CRPS | 2.83 (3.35) | 1.65 (4.69) | 2.86 (3.73) |
| | SSREL | 1.31 (2.61) | 0.33 (3.54) | 1.03 (2.44) |
| | RMSE | 4.52 (5.34) | 2.61 (6.99) | 4.83 (5.95) |
| | MAE | 3.67 (4.25) | 2.15 (5.76) | 3.75 (4.74) |
| Baseline | CRPS | 3.23 (3.48) | 2.26 (4.83) | 3.45 (3.90) |
| | SSREL | 1.89 (2.45) | 0.67 (4.19) | 1.17 (2.76) |
| | RMSE | 5.35 (5.68) | 3.67 (7.17) | 5.54 (6.09) |
| | MAE | 4.28 (4.56) | 2.96 (6.00) | 4.31 (4.93) |

Table 2. Prediction skills of the best VED and the best baseline model on the Maria experiments.

| Experiment | Metric | Training | Validation | Test |
|------------|--------|--------------------|--------------------|--------------------|
| VED | CRPS | 1.76 (5.88) | 2.28 (7.78) | 1.39 (5.26) |
| | SSREL | 0.59 (3.51) | 0.80 (4.33) | 0.33 (2.95) |
| | RMSE | 3.74 (9.27) | 3.93 (10.12) | 2.21 (7.32) |
| | MAE | 2.21 (7.95) | 3.20 (9.95) | 1.74 (7.08) |
| Baseline | CRPS | 1.16 (2.32) | 2.39 (3.46) | 2.32 (2.60) |
| | SSREL | 0.36 (1.62) | 0.88 (3.28) | 1.68 (2.21) |
| | RMSE | 2.46 (4.57) | 3.57 (6.22) | 3.54 (3.84) |
| | MAE | 2.03 (3.21) | 3.13 (4.85) | 3.22 (3.51) |

4.2 Prominence of Radiative Feedbacks in the Early Intensification Phase

4.2.1 Identifying Periods of Radiatively-Driven Intensification

By construction, our simple VED model predicts TC intensification exclusively from radiative heating, overlooking significant contributions from surface fluxes and wind-induced surface heat exchange (Zhang & Emanuel, 2016; Murthy & Boos, 2018). Recent modeling studies (e.g., Smith et al., 2020; Yang & Tan, 2018) suggest that radiative heating could be less critical to TC intensification beyond the initial genesis or spin-up stage.

To investigate whether this holds in our case studies, we use the VED model to *identify periods when radiative feedbacks dominate TC intensification*. Instances with significant model errors or uncertainties are times when radiative heating alone cannot predict TC intensification. In contrast, instances with accurate predictions and minimal uncertainty are likely times when radiative heating is dominant.

Our VED’s capability to distinguish radiative heating-dominated stages is crucial for reliability assessment and scientific discovery. Figure 3 presents the mean prediction and prediction spread of the best-calibrated VED models for Haiyan and Maria. For Maria, the probabilistic ML models replicate the intensification rate reduction in CRF mechanism-denial experiments (Fig. 3a). Decomposing predicted intensification into longwave and shortwave contributions (Fig. 3b) shows that the slower intensification in the mechanism-denial experiments is primarily attributable to the longwave component. This result is reassuring as it identifies the longwave component of CRF as the main contributor to the early intensification of TCs, consistent with the “cloud greenhouse effect” framework in Ruppert et al. (2020). However, the model underestimated the intensification rate at the latter stage of the NCRF-60h TC’s life cycle, possibly due to unaccounted non-radiative processes like the surface fluxes feedback (e.g., Zhang & Emanuel, 2016). Furthermore, the model assigned a smaller weight to the shortwave channel in the linear prediction equation for Maria (Fig. 3b), resulting in a shortwave contribution close to zero. We believe the model has learned the strong effect of disabling CRF in the sensitivity experiments and its impact on intensification, which manifests mainly in the longwave channel. The shortwave contribution is larger in the realistic Haiyan ensemble simulations (Fig. 3d).

For Haiyan, where CRF always exists, we compare the VED predictions for a high intensification rate Haiyan ensemble member (Member 2) to those for a slow intensification member (Member 11) to assess the role of radiation in realistic conditions (Fig. 3c). Increased bias (Fig. 3c) and wider uncertainty range (Fig. 3e) for Member 2 predictions in the latter part of the TC’s life cycle shows the limitation of the VED model to understand the mature phase of TC intensification. The prediction distribution for sam-

ples taken during the high uncertainty phase is close to the training data distribution (prior), implying the need for non-radiative inputs to adequately constrain the probabilistic predictions and reduce overall model bias. In contrast, the model predictions for samples taken from the early intensification phase of Member 2 are accurate, indicating predictability from the radiative heating fields.

Comparing linear decompositions of VED predictions (Fig. 3d) reveals that lower intensification rates for Member 11 (Hours 10-20) are due to reduced longwave contribution. Positive longwave contribution in Member 2 leads to a faster intensification rate beyond the persistence baseline (overall model bias). In the next section, we analyze the radiation structures in the two ensemble members to provide physical interpretations of how differences in radiative heating structures might explain the differing intensification rates of the two ensemble members.

4.2.2 Qualitative Agreement with Existing Diagnostic Tools

In the previous section, we claimed that transitioning from an accurate, low-uncertainty regime to an inaccurate, high-uncertainty regime in the VED predictions can be understood as separating periods where radiation is more critical from non-radiative processes are more important. Here, we use well-established budget analysis tools to evaluate the extent to which the claim is valid.

We can analyze the cyclogenesis process with the Frozen Moist Static Energy Spatial Variance Budget (Wing & Emanuel, 2014; C. J. Muller & Romps, 2018; Carstens & Wing, 2020):

$$\frac{1}{2} \frac{\partial \text{var} \hat{h}}{\partial t} = \underbrace{\overline{\hat{h}' \text{LHF}'} + \overline{\hat{h}' \text{SHF}'}}_{\text{SEF Contribution}} + \underbrace{\overline{\hat{h}' \text{NetLW}'} + \overline{\hat{h}' \text{NetSW}'}}_{\text{Radiative Contribution}} - \overline{\nabla_h \cdot \hat{u} \hat{h}}, \quad (22)$$

where $\text{var} \hat{h}$ is the spatial variance of vertically integrated moist static energy (MSE), and SEF (the Surface Enthalpy Flux) is the sum of LHF (the Latent Heat Flux) and SHF (the Sensible Heat Flux). The radiative contribution consists of net column longwave radiative flux convergence (NetLW) and net column shortwave radiative flux convergence (NetSW). Primes indicate anomalies relative to the mean of the spatial domain, represented by overlines. MSE spatial variance source terms are obtained by spatially averaging all terms on the right-hand side of Equation 22. We perform the spatial averaging from 0 to 600 km from the TC center. The MSE variance summarizes the spatial distribution of frozen MSE surrounding a developing tropical cyclone, with the biggest contribution coming from moisture (Carstens & Wing, 2022). Since tropical cyclogenesis shares similarities with rotating convective self-aggregation, TCs form as the TC thermodynamics transition to an aggregated state, characterized by a compact moisture blob surrounded by drier air (positive $\partial_t \text{var} \hat{h}$, e.g., C. J. Muller & Romps, 2018; Carstens & Wing, 2020). From Equation 22, the source terms for the MSE variance are the covariance between the existing MSE anomalies and different flux anomalies. Creating positive MSE variance anomalies necessitates spatially-aligned anomalies. For example, positive radiative contribution to MSE variance may arise from warm longwave heating anomalies in the high energy TC inner core or cool radiative anomalies in the drier TC surroundings (Nicholls, 2015). Inward moisture transport from radiatively-driven secondary circulations (in-up-out circulations; e.g., Nicholls, 2015; Ruppert et al., 2020; Smith et al., 2020) can enhance MSE variance by redistributing moisture towards the TC center.

Fig 3e compares the time evolution of the radiation and surface enthalpy flux MSE variance source terms and the time evolution of the learned logarithmic variance structure for the longwave channel ($\log \sigma_{LW}^2$). The advection term is not considered due to the coarse temporal resolution of the saved WRF outputs. Focusing on Haiyan member 2, the contribution from NetLW to the overall MSE variance budget is initially com-

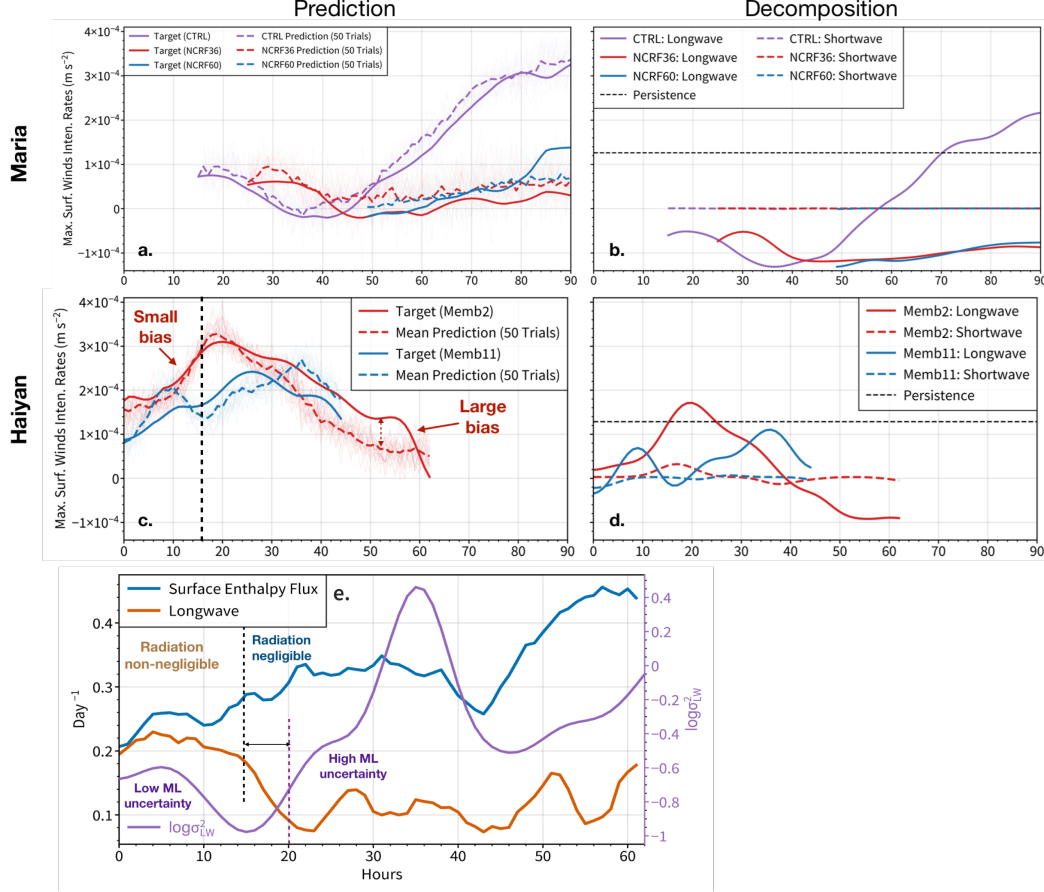


Figure 3. Decomposing tropical cyclone intensification predictions for Maria and Haiyan shows longwave radiative heating’s link to early intensity differences. We present mean VED surface intensification predictions (dashed) for Maria (a) from three WRF simulations and for Haiyan (c) from two ensemble members, with actual intensities (thick). The shadings in the left columns illustrate the range of possible VED predictions given the same inputs using a Monte Carlo approach. Panels (b) and (d) show longwave and shortwave radiation contributions to the mean VED predictions. Zooming in on Haiyan Member 2, Panel (e) compares the evolution of VED uncertainty associated with longwave radiation (purple) against two MSE variance sources (blue and brown). In Maria’s mechanism-denial experiment and the early phase of Haiyan, the model associates the difference between a quickly intensifying TC and a slowly intensifying one with longwave radiation.

. The vertical dashed lines in panel (e) show the two-stage behavior in the longwave MSE variance source term (black) and similar behavior in VED prediction uncertainties (purple). The time lag between the two methods is shown in panel (e; black arrow).

parable to the contribution from SEF but becomes less important towards the end of the time series. This behavior is consistent with the expected increase in prominence of surface fluxes feedback (WISHE; Emanuel, 1986; Rotunno & Emanuel, 1987; Zhang & Emanuel, 2016) after the initial genesis stage. Consistent with the MSE variance budget analysis, we see two distinct phases in the $\log \sigma_{LW}^2$ time series, one with smaller values before 20h (fewer prediction uncertainties) and one with larger values after 20h (more prediction uncertainties). It is encouraging that the NetLW term and $\log \sigma_{LW}^2$ time series have a two-stage behavior as it ensures that the ML model is trustworthy and has learned physically meaningful relationships.

A notable caveat to the above discussion is that our ML framework predicts TC kinematic changes, whereas the MSE variance budget measures thermodynamical changes. This distinction potentially explains a 5-hour time lag between the decrease in longwave contribution to MSE variance and the increase in ML prediction uncertainties. The idea that thermodynamic forcing precedes kinematic changes can be supported by Figure 2 in Ruppert et al. (2020), where TC surface intensification occurs 12-24 hours after the drop in SEF contributions. The analysis in Tang (2017) also shows that strong moist entropy forcing precedes the genesis time of idealized axisymmetric TCs. Finally, airborne observations suggest that the TC core becomes and remains close to saturation for some time before the build-up of storm circulations (Bell & Montgomery, 2019).

4.3 Axisymmetric results: The dominance of upper-level longwave radiation

The proposed framework’s physical interpretability relies on the model predictions and the extracted structures. In the following sections, we progressively highlight different aspects of the extracted structures to show how they can clarify the role of radiation in TC intensification. We start by analyzing the azimuthal mean of VED-extracted structures to illustrate how spatial gradients in radiative anomalies affect TCs. We obtain these structures by multiplying the PCA spatial modes and the trained encoder weights.

4.3.1 *Maria*

In the case of the Maria simulations (Figure 4), the VED model extracts a μ_{LW} pattern with an upper-level longwave anomaly dipole and a shallow cloud radiative signal near the surface (Figure 4c). The anomaly fields are defined with respect to the training mean. In other words, it shows how the radiative heating structure of a sample deviates from the mean of all training samples. This way of defining the anomaly also eliminates the need to recalculate the PCs for individual experiments. To demonstrate how the learned $\Pi_{\mu_{LW}}$ (Fig. 4c) encodes physical knowledge, we compare Hour 80 from the Maria CTRL simulation (Fig. 4a, b) to a sample taken from the same time in the NCRF-36h experiment (Fig. 4d, e). The VED framework predicts higher surface intensification rates for the CTRL sample due to positive μ_{LW} . In contrast, the NCRF-36h sample has a lower predicted intensification rate due to negative μ_{LW} . Comparing Figure 4b and c, we see that a positive μ_{LW} arises when the anomaly field is spatially distributed in the same way as $\Pi_{\mu_{LW}}$. In the raw longwave radiation field (Fig. 4a), the positive μ_{LW} of the CTRL sample corresponds to the concentration of strong longwave cooling near the cloud top (i in Fig. 4a) and heating near the TC center (ii in Fig. 4a). In contrast, the negative μ_{LW} in the mechanism denial example features a lowered and weakened longwave cooling and the absence of heating near the TC center; both contribute to a weaker simulated TC. From the Maria example, we demonstrate that combining the sign of the projection (μ_{LW}) and the raw fields provides valuable information on why NCRF-36h TC fails to intensify. The next section uses μ_{LW} to understand why two Haiyan ensemble members have different intensification rates during their organization phases.

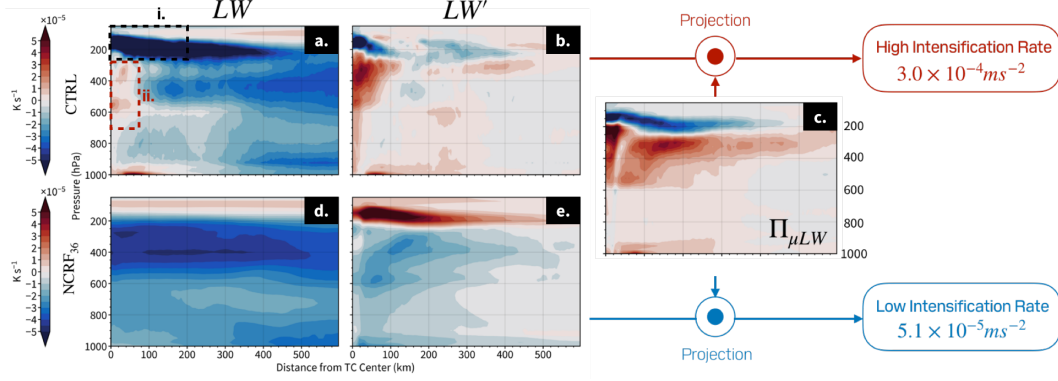


Figure 4. The learned data-driven structure for the mean longwave prediction ($\Pi_{\mu LW}$; c) for Maria shows a prominent upper-level longwave anomaly dipole. A sample from Hour 80 of the CTRL simulation (a-b), which is predicted by the ML model to have a high intensification rate because of a positive projection of LW' (b; perturbation compared to the training mean) onto $\Pi_{\mu LW}$ (c). We contrast the CTRL sample with another sample taken at the same hour from the NCRF-36h simulation (d-e), which is predicted to have a negative intensification rate due to a negative projection of LW' (e) onto $\Pi_{\mu LW}$. The two samples illustrate the physical meaning of the projections: a positive projection (red arrows) occurs when the LW' is similarly spatially to $\Pi_{\mu LW}$, whereas a negative projection occurs when the LW' is opposite in sign to $\Pi_{\mu LW}$.

4.3.2 Haiyan

The azimuthal mean of μ_{LW} for Haiyan (Fig. 5c) exhibits a vertical dipole pattern around 200 hPa and a shallow vertical dipole at 900 hPa, reflecting broad anvil clouds in the outer core and shallow clouds in the inner core. We compare samples from two members: Member 2, with a significant positive μ_{LW} (larger predicted intensification rate), and Member 11, with a small μ_{LW} (smaller predicted intensification rate). In the Member 2 sample, positive μ_{LW} indicates weakening of the upper-level longwave dipole between 50 km to 300 km from the TC center and a vertically expanded upper-level longwave heating near the TC center (i in Fig. 5a), along with a more prominent 900 hPa shallow cloud radiative dipole (ii in Fig. 5a). These longwave patterns may indicate deep convective development, rising outflow height near the TC center, destabilized inner core upper-level thermal stratification, and enhanced shallow cloud frequency. Colder upper tropospheric temperatures and higher outflow layers have been shown to boost TC intensity. Following balanced dynamics (Eliassen, 1952; Pendergrass & Willoughby, 2009), upper-level radiative cooling triggers secondary circulations that accelerate surface tangential winds in idealized TCs (Trabing et al., 2019). From an energetic perspective, rising outflow layers enhance the thermal efficiency of a TC heat engine, resulting in a stronger TC (Ramsay, 2013; S. Wang et al., 2014). While shallow clouds are suggested to assist cyclogenesis by moistening the lower troposphere and spinning up the near-surface circulation (Z. Wang, 2014), our VED model analysis implies their effect on the overall TC intensification is relatively minor. Decomposing the model prediction by vertical level (description in Appendix C) suggests that the shallow cloud contribution to intensification is between two and one order of magnitude smaller than the upper-level radiative contribution (Fig. 7b). These findings corroborate those from idealized simulations (e.g., Kilroy, 2021).

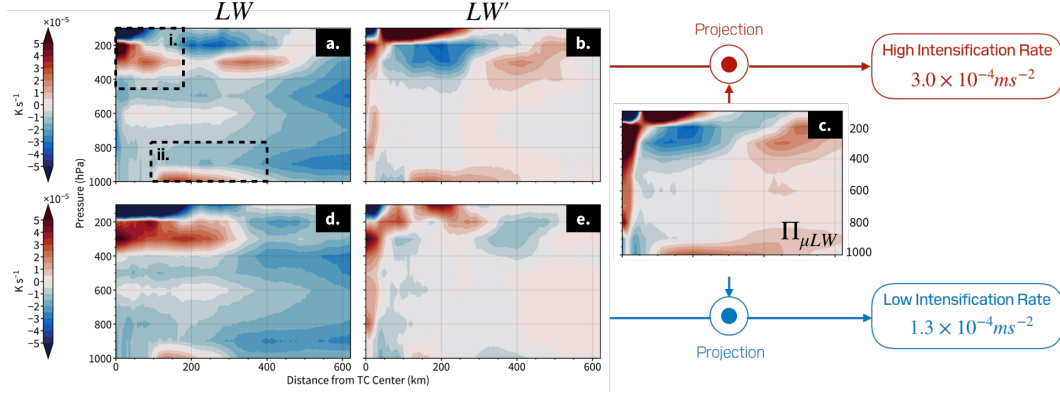


Figure 5. The learned data-driven structure for the mean longwave prediction ($\Pi_{\mu LW}$; c) for Haiyan shows the spatial distribution of LW' that is most correlated with early TC intensification. The example that is predicted to have a high intensification rate (a,b) is taken from Hour 15 of Member 2, whereas the predicted low intensification rate (d,e) example is taken from Hour 17 of Member 11. The Member 2 LW' example has a strong positive projection (red arrows) onto $\Pi_{\mu LW}$ (c), which is indicative of concentrated inner-core deep convection (200 hPa longwave anomaly dipole within 100 km of TC center) in the raw azimuthal-averaged LW. Additionally, the Member 2 example also features shallow clouds in the outer core (900 hPa anomaly dipole between 100-300 km from the TC center; b). Both the inner-core deep convection and outer-core shallow cloud signatures are weaker in the Member 11 example, which leads to a lower predicted intensification rate (blue arrow).

4.4 Asymmetric Radiative Heating favors Tropical Cyclone Intensification

Here, we show that some asymmetric longwave radiative anomaly structures are potential predictors for intensification. The linear combinations of PC longwave eigenvectors yield a complex, spatially asymmetric, three-dimensional radiative heating pattern (Fig. 6a,b). The $\Pi_{\mu LW}$ cross sections at 1000 hPa (Fig. 6a) and 100 hPa (Fig. 6b) both exhibit distinct wavenumber-1 asymmetry, with a shallow cloud radiative signature at 1000 hPa (i. in Fig. 6a; downshear right quadrant) distributed upwind of the deep convective signature at 100 hPa (ii. in Fig. 6b; downshear left quadrant). Considering how the secondary circulations associated with CRF may intensify tangential winds and spin up surface cyclones (Ruppert et al., 2020), we postulate that any positive longwave contribution to Member 2 surface winds should be distributed mainly in the TC's northern half. We validate this with the surface wind intensification from Hour 16 to 40 (Fig. 6c), which shows the effect of a positive μ_{LW} . The surface wind acceleration is indeed broader over the TC's northern half, with the strongest acceleration located downwind of the downshear left positive upper-level $\Pi_{\mu LW}$ with minimal uncertainty. The spatial correlation between surface wind acceleration and $\Pi_{\mu LW}$ supports the hypothesis that upper-level wavenumber-1 longwave heating anomaly contributes positively to surface intensification. While shallow clouds have a minor contribution to the overall TC intensification (Section 4.2), the shallow cloud radiative signature (i in Fig. 6a) still coincides spatially with the intensifying *local* winds in the downshear right quadrant.

To identify which mesoscale anomalies in $\Pi_{\mu LW}$ are most unambiguously correlated to intensification, we create standard deviation maps from the ten best-performing models' $\Pi_{\mu LW}$ structures (Fig. 6d,e). Low standard deviations suggest that the ML models consistently find the exact relationship between mesoscale anomalies and intensifi-

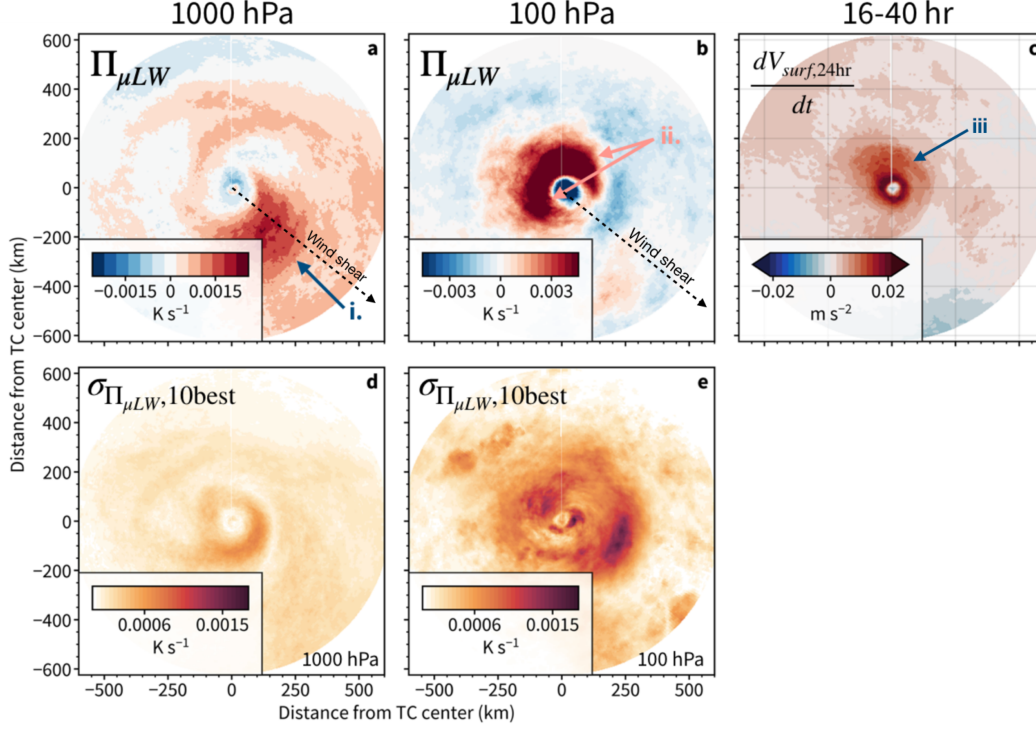


Figure 6. The spatial cross-sections of the best-performing model’s mean longwave pattern $\Pi_{\mu LW}$ at (a) 1000 hPa and (b) 100 hPa both exhibit substantial wavenumber-1 asymmetry in the inner core (0-200 km from the TC center). The trustworthiness of individual anomaly areas in $\Pi_{\mu LW}$ is assessed by the standard deviation of the 10 best models’ $\Pi_{\mu LW}$ at (c) 1000 hPa and (d) 100 hPa. We highlight two longwave anomalies that are trustworthy (small $\Pi_{\log \sigma^2 LW}$): a low-level shallow cloud signature (i in a) and the deep convection downwind of the shallow cloud signature (ii in b). We compare (c) the 24-hr surface wind intensification associated with the Member 2 example in Figure 5a-b to show a strong spatial correlation between the broad surface wind intensification (iii in c) and the upper-level longwave anomaly signature (ii in b).

cation in a specific area. We should prioritize such areas in our analysis. Using the deviation maps at 100 hPa (Fig. 6e), we conclude that the 100 hPa $\Pi_{\mu LW}$ positive anomaly in the downshear left quadrant (i in Fig. 6a) is unambiguously related to intensification (low uncertainty). In contrast, the upper-level anomalies in the upshear quadrants have more uncertainty. Similarly, the 1000 hPa deviation map (Fig. 6d) shows model consistency in depicting a cold LW anomaly at the TC center and a shallow cloud signature in the downshear right quadrant (i in Fig. 6a). A high standard deviation in the boundary between the two areas indicates uncertainty in the spatial extent of these signatures across models (Fig. 6d).

Considering these results, the longwave anomaly signature associated with deep convection in the downshear left quadrant is the feature that has the strongest correlation to surface intensification. Widespread inner core convective development near and slightly downwind of the upper-level longwave anomalies (not shown) in the Haiyan Member 2 example points to a link between longwave anomalies, secondary circulations, and deep convective development, which also facilitate the axisymmetrization of TC structures - an indicator of TC genesis (Hendricks et al., 2004) and intensification (Shimada et al., 2017).

5 Discussion

5.1 Complementing Physics-Based Budget Analysis with Machine Learning Diagnostics

This section briefly discusses how the proposed ML-based method complements existing physics-based diagnostic methods. The first category of physics-based diagnostic methods is budget equations. Budget equations are attractive in that each term in the equation has a well-defined physical meaning; the equations suitable for the tropical cyclogenesis problem include the moist static energy variance budget (Wing & Emanuel, 2014), horizontal momentum budget (Huang et al., 2018), kinematic energy budget (Y. Wang et al., 2016), and available potential energy budget (Novak & Tailleux, 2018). One disadvantage of budget analyses for our problem is that they do not directly predict surface intensification from thermal forcing. The MSE variance budget calculates the spatial variance in MSE (a thermodynamic term), whereas the horizontal momentum equation lacks a thermal source term. There is no direct equation that links the MSE variance and TC intensity, even though a statistical correlation exists between the two (Wing, 2022). While it is possible to get physical insights by comparing the thermodynamic and kinematic budget terms side-by-side, such analyses are qualitative, not quantitative. Another disadvantage common to all budget analysis methods is that they rely on variables not typically included in simulation output lists. It is well-known that these budgets are hard to close *post-hoc* (Chen et al., 2020), i.e., calculating the budget terms with typical model outputs, especially if the model outputs are stored infrequently. A better option is to estimate those terms directly in the model (online). However, this requires re-running pre-existing large cloud-resolving simulation datasets with the online calculation of budget terms (e.g., Stevens et al., 2019), which is often computationally prohibitive. Hence, our ML framework complements physics-based budgets by (i) establishing quantitative relationships between thermodynamic forcing and kinematic changes and (ii) relaxing the data requirements in temporal frequency and online budget calculations.

The second category of physics-based diagnostics used in tropical cyclogenesis studies is the Sawyer-Eliassen Equation (SEQ; Pendergrass & Willoughby, 2009). Given a thermodynamic forcing, the SEQ outputs a streamfunction representing the balanced circulation induced by said heating. While this method links thermodynamics and kinematics, the physical assumptions used to derive the SEQ (hydrostatic, thermal wind balance) mean that the thermal forcing needs to be averaged over a long period of time. Additionally, the SEQ only provides the 2D solutions for azimuthally-averaged 2D thermal forcing in radius-height coordinates, which removes crucial spatial context. Finally, Bui et al. (2009) noted that the balance solution substantially underestimates the boundary layer inflow, which is problematic for surface intensity assessments. While an unbalanced version of the SEQ exists (Ji & Qiao, 2023), the extended SEQ is still a 2D diagnostic framework. Following the above discussions, our ML method complements SEQ by allowing 3D thermal forcing as an input, which enables analyses of the effect of asymmetric thermal forcing on surface winds (Section 4.3).

Our ML framework extracts one time-invariant pattern per variable. The intensification rates predicted by the framework are linearly related to the spatial similarities between the radiative structures of individual samples and the extracted pattern. Our approach complements traditional composite analysis by removing subjectivity in the definition of composites. Finally, our framework highlights specific small-scale anomalies most relevant to information by enabling quantifiable assessments of each anomaly’s contribution to ML predictions.

5.2 Anticipating the Response of Tropical Cyclones to Radiative Perturbations

One of the main advantages of ML models compared to traditional physics-based models is that ML models are inexpensive to run once they are trained. We may leverage this characteristic of ML models for scientific discovery. Specifically, we may treat ML models as an efficient hypothesis generator and a framework for simple hypothesis testing.

We design a sensitivity experiment using the trained Haiyan models to understand whether the prominent wavenumber-1 structure in μ_{LW} means that asymmetric long-wave anomaly is more critical to intensification than axisymmetric ones. These questions are easily answerable by feeding the ML models with perturbed input, i.e., synthetic structures. Here, we present the full definition of axisymmetric and asymmetric anomalies used in the intervention experiments.

Taking longwave radiation as an example, its mean contribution to the ML intensification forecast is proportional to $\mu_{LW}(t)$ (Eq. 9). We would like to show that adding an asymmetric pattern like $\Pi_{\mu_{LW}}$ causes the ML model to predict higher intensification rates than adding an axisymmetric pattern. In the asymmetric pattern experiment, we perturb the raw data in cartesian coordinates by adding the learned pattern to the training-mean longwave cooling field:

$$\overline{LW_{training}} \pm \Pi_{\mu_{LW}}, \quad (23)$$

which tests the effect of adding or removing extra radiation to specific areas in the developing TC. For the case of the axisymmetric pattern experiment, we perturb the raw data with the azimuthal mean of the extracted μ_{LW} pattern:

$$\overline{LW_{training}} \pm \gamma \overline{\Pi_{\mu_{LW}}}^{\theta}, \quad (24)$$

where γ is a multiplication factor that ensures that both synthetic structures have the same spatial variance and $(\cdot)^{\theta}$ is the azimuthal mean operator. Practically, every grid point in the axisymmetric synthetic structure is multiplied by the ratio between the standard deviation of the asymmetric and axisymmetric synthetic structure.

Feeding the VED with the new inputs perturbed by the synthetic asymmetric structure predicts higher longwave contributions to intensification during the early intensification stage. Conversely, the axisymmetric synthetic structure leads to a smaller response in the VED prediction (Fig. 7a). VED predictions are only weakly sensitive to the synthetic perturbations later in the TC's life cycle. These results broadly agree with our conjecture that asymmetric longwave forcing leads to faster early TC intensification in the data-driven models.

6 Conclusion

Recent evidence (e.g., Ruppert et al., 2020) highlights the significance of radiation in early TC development. However, the precise role of radiation in realistic TCs and whether asymmetric structures in radiation impact TCs differently from axisymmetric ones has remained underexplored. We fill this knowledge gap by employing a data-driven, interpretable, stochastic, machine learning model (VED) on convective-permitting simulations of two TCs to estimate the transfer function between 3D radiative patterns and surface wind intensification. We optimize the model architecture to enhance the likelihood of extracting physically meaningful patterns. This optimization involves (i) maximizing surface intensification prediction skills by optimally combining different asymmetric radiative patterns and (ii) regressing to the unconditional distribution of intensification rates when radiation is uninformative. In both case studies, our model finds

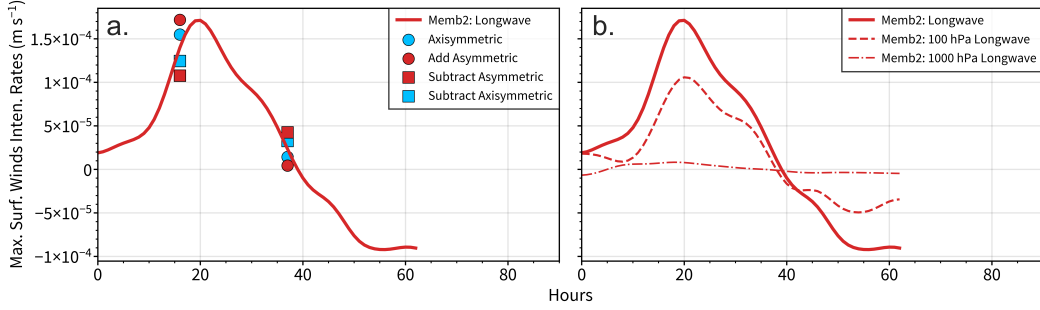


Figure 7. Providing the trained ML models with perturbed inputs gives us the first hints as to how the tropical cyclones might behave in a true intervention setting. Panel (a) shows how perturbing the Haiyan Member 2 at Hour 15 with the asymmetric $\Pi_{\mu LW}$ (red dots and squares) changes the longwave contribution to the ML prediction (red line) compared to perturbing the same sample with an axisymmetric version of $\Pi_{\mu LW}$ (blue dots and squares). Panel (b) shows that upper-level anomalies (100 hPa; dashed red) contributes more to the overall longwave contribution (red line) than the lower tropospheric anomalies (1000 hPa; dashed dotted red).

spatially coherent, physically meaningful radiation patterns from complex, high-dimensional simulation output data.

The VED architecture allows the quantification of uncertainties in both the model predictions and the extracted radiation patterns. We provide several examples where we leverage this information for scientific discovery. By intentionally making the model learn exclusively from radiation, the errors and uncertainties in ML predictions are quantifiable indicators of how relevant radiation is to TC intensification. Our findings reveal that longwave radiation exerts a larger influence on intensification than shortwave. The radiation is mostly only relevant in the early genesis phase (Section 4.2), consistent with the results from prior physical modeling experiments.

The ML model extracts three-dimensional structures in radiation and quantifies the effect of different radiative anomalies on intensification. Our results suggest that the combination of downshear left deep convective development in the inner core and low tropospheric shallow clouds in the downshear right quadrant may be used as valuable predictors for the rate of intensification during the TC genesis phase (Section 4.4). The deep convective and shallow cloud signals have a wavenumber-1 spatial asymmetry. Our VED model’s linearity is useful here because we can, e.g., decompose by vertical level to conclude that the upper-level radiative signal likely impacts the surface intensification the most. The VED-extracted three-dimensional longwave anomaly structure for Haiyan has a strong spatial correlation with the broader surface wind intensification in the northern quadrants, which is potentially helpful to highlight where longwave radiative anomalies should be distributed that can potentially yield the most impact on TC intensification.

We believe that the strength of the ML framework here lies in its simplicity. The entirely linear nature of the model ensures full interpretability and decomposability, providing clarity on how the model extracts structures from WRF outputs. Our case studies demonstrate the value of sacrificing some model performance for interpretability and how interpretability leads to scientific discovery. The simple linear VED models also show superior skills to the more complex ML models in low sample size regimes (Section 4.1). Our approach is a valuable addition to existing data-driven approaches for scientific exploration and is particularly useful in situations with limited training data. The archi-

texture is flexible, allowing for an easy introduction of nonlinearity and making it adaptable to other prediction problems in more complex systems.

Looking ahead, interpretable ML architectures can potentially be used to (i) reveal the source of forecast spreads in ensemble model predictions for extreme winds, e.g., by identifying the dominant uncertainty-adding circulation patterns, and (ii) quantifying the impact of different physical variables on uncertainties in climate models. We can also adopt the framework to forecast the spin-up of local winds in different shear-relative quadrants for a clearer understanding of the role of radiation in the genesis of TCs. Finally, a logical next step to build trust in the ML model explanations is to use the learned structures for targeted sensitivity experiments with physics-based numerical models, which should clarify the causal relationship between these structures and TC intensification.

7 Open Research

The code used to train the neural networks and to produce all figures of this manuscript is hosted on Github (https://github.com/freddy0218/2024_TCG_VED) and stored in a DOI-assigned public repository (Tam, 2024a). The processed PC time series data and trained models are archived on a separate, DOI-assigned public repository (Tam, 2024b). The post-processed longwave and shortwave WRF radiation fields for the two Haiyan ensemble members are also included in the archive for recreating the results shown in Figure 3 and 5. All WRF namelist settings files to recreate the WRF simulations used in this study are archived in a separate repository (Ruppert, 2024) with postprocessing scripts. The PyTorch (Paszke et al., 2019) framework is used to train all the machine learning models in this manuscript. The binary files of PyTorch are available for installation via the Anaconda platform. The Optuna optimization tool can be accessed on <https://github.com/optuna/optuna>. We provide a short Jupyter tutorial with the minimal steps required to use the trained models to get the intensification rate predictions and the extracted mean longwave structure. This file can be assessed from the repository (Tam, 2024b) (minimalexample.ipynb).

Acknowledgments

This research was supported by the canton of Vaud in Switzerland. J.H.R. acknowledges funding support from the National Science Foundation under grants AGS 1712290 and 2331120. The authors acknowledge the Scientific Computing and Research Support Unit (DCSR) and Margot Sirdey at the University of Lausanne for providing the necessary computational resources and technical support. The authors also acknowledge Saranya Ganesh S., Milton Gomez, Louis Poulain-Auzéau, Allison A. Wing, and Caroline Muller for fruitful discussions at different stages of this manuscript’s conceptualization.

Appendix A Derivation steps for the Effective Weights, Biases, and Constants

This appendix presents the relevant steps to derive the Effective Weights and bias of the overall VED model (Sections 3.2.2, 3.2.3), followed by the scaling factors and logarithmic variance constants.

We first focus on the model bias term. The decoding (prediction) module of the VED model can be mathematically expressed by:

$$\begin{aligned} \left(\frac{dV_{surf}}{dt} \right)_{24hr} &= a_{2,LW} \mathcal{N} \left(\mu_{LW}, e^{\log \sigma_{LW}^2} \right) \\ &+ a_{2,SW} \mathcal{N} \left(\mu_{SW}, e^{\log \sigma_{SW}^2} \right) \\ &+ b_2. \end{aligned} \tag{A1}$$

We expand A1 with 5 and 6, the mean structure scalars (μ_{LW}, μ_{SW}) in A1 becomes:

$$\begin{aligned}\mu_{LW} &= a_{2,LW} \left(b_{1,LW,\mu} + \sum_{i=1}^{n_{LW}} \frac{a_{1,LW,\mu,i}}{\sigma(PC_{i,LW})} PC_{i,LW} - \sum_{i=1}^{n_{LW}} \frac{a_{1,LW,\mu,i}}{\sigma(PC_{i,LW})} \overline{PC_{i,LW}} \right), \\ \mu_{SW} &= a_{2,SW} \left(b_{1,SW,\mu} + \sum_{i=1}^{n_{SW}} \frac{a_{1,SW,\mu,i}}{\sigma(PC_{i,SW})} PC_{i,SW} - \sum_{i=1}^{n_{SW}} \frac{a_{1,SW,\mu,i}}{\sigma(PC_{i,SW})} \overline{PC_{i,SW}} \right).\end{aligned}\quad (\text{A2})$$

The overall bias (b) of the VED model is the sum of the first and third terms in Eqs. A2.

Comparing Equations 11, A1, and A2 shows that the non-constant terms (second on the right-hand side) in Equation A2 is equivalent to the projection of radiative anomaly onto the learned patterns (Eqs. 10). Using longwave mean structure as an example, we have:

$$PC_{i,\Pi_{LW,\mu}} = \lambda \frac{a_{2,LW} a_{1,LW,\mu,i}}{\sigma(PC_{i,LW})}, \quad (\text{A3})$$

where λ is the proportionality coefficient for the longwave mean structure. We now assume the norm of the data-driven structure to be 1:

$$1 = \langle \Pi_{LW,\mu} | \Pi_{\mu LW} \rangle_{LW} = \sum_{i=1}^{n_{LW}} PC_{i,\Pi_{LW,\mu}}^2 = \lambda^2 a_{2,LW}^2 \sum_{i=1}^{n_{LW}} \frac{a_{1,LW,\mu,i}^2}{\sigma(PC_{i,LW})^2}, \quad (\text{A4})$$

From Equation A4, the λ for longwave mean structure is:

$$\lambda_{LW,\mu} = \left[|a_{2,LW}| \sqrt{\sum_{i=1}^{n_{LW}} \frac{a_{1,LW,\mu,i}^2}{\sigma(PC_{i,LW})^2}} \right]^{-1}. \quad (\text{A5})$$

The other three λ in the VED model can be obtained with a similar procedure.

We can rewrite Equation A1 with the definition of the mean structure scalars (Eqs. A2), Equations 6, and λ (Eq. A5),

$$\begin{aligned}\left(\frac{dV_{surf}}{dt} \right)_{24\text{hr}} &= \mathcal{N} \left(\underbrace{\frac{a_{2,LW}}{\lambda_{LW,\mu}} \sum_{i=1}^{n_{LW}} PC_{i,\Pi_{\mu LW}} PC_{i,LW}}_{\langle LW | \Pi_{\mu LW} \rangle}, \sqrt{a_{2,LW}} e^{\log \sigma_{LW}^2} \right) \\ &+ \mathcal{N} \left(\underbrace{\frac{a_{2,SW}}{\lambda_{SW,\mu}} \sum_{i=1}^{n_{SW}} PC_{i,\Pi_{\mu SW}} PC_{i,SW}}_{\langle SW | \Pi_{\mu SW} \rangle}, \sqrt{a_{2,SW}} e^{\log \sigma_{SW}^2} \right) \\ &+ b\end{aligned}\quad (\text{A6})$$

To see how Equation A6 related to Equation (11), we factor out all constant terms from the normal distribution:

$$\begin{aligned}\left(\frac{dV_{surf}}{dt} \right)_{24\text{hr}} &= \underbrace{\frac{a_{2,LW}}{\lambda_{LW,\mu}}}_{a_{LW}} \mathcal{N} \left(\langle LW | \Pi_{\mu LW} \rangle_{LW}, \sqrt{\lambda_{LW,\mu} |a_{2,LW}|} e^{\log \sigma_{LW}^2} \right) \\ &+ \underbrace{\frac{a_{2,SW}}{\lambda_{SW,\mu}}}_{a_{SW}} \mathcal{N} \left(\langle SW | \Pi_{\mu SW} \rangle_{SW}, \sqrt{\lambda_{SW,\mu} |a_{2,SW}|} e^{\log \sigma_{SW}^2} \right) \\ &+ b,\end{aligned}\quad (\text{A7})$$

allowing us to identify the “effective weights” a_{LW} and a_{SW} .

We now use the definition of the logarithmic variance in the model’s first (projection) layer (6) to expand the logarithmic variance term of the normal distributions:

$$\sqrt{\lambda_{LW,\mu} |a_{2,LW}|} \exp(\log \sigma_{LW}^2) = \sqrt{\lambda_{LW,\mu} |a_{2,LW}|} \exp \left(b_{1,LW,\log \sigma^2} + \sum_{i=1}^{n_{LW}} a_{1,LW,\log \sigma^2,i} \times \widetilde{PC}_{i,LW} \right) \quad (\text{A8})$$

$$\sqrt{\lambda_{SW,\mu} |a_{2,SW}|} \exp(\log \sigma_{SW}^2) = \sqrt{\lambda_{SW,\mu} |a_{2,SW}|} \exp \left(b_{1,SW,\log \sigma^2} + \sum_{i=1}^{n_{SW}} a_{1,SW,\log \sigma^2,i} \times \widetilde{PC}_{i,SW} \right) \quad (\text{A9})$$

We notice that parts of Equation A8 and A9 are constant, which means that we can simplify this equation further by defining variance prefactors for longwave radiation (c_{LW} ; Eq. 16) and shortwave radiation (c_{SW} ; Eq. 17).

$$c_{LW} = \sqrt{\lambda_{LW,\mu} |a_{2,LW}|} \exp \left(b_{1,LW,\log \sigma^2} - \sum_{i=1}^{n_{LW}} a_{1,LW,\log \sigma^2,i} \frac{\overline{PC}_{i,LW}}{\sigma(PC_{i,LW})} \right), \quad (\text{A10})$$

$$c_{SW} = \sqrt{\lambda_{SW,\mu} |a_{2,SW}|} \exp \left(b_{1,SW,\log \sigma^2} - \sum_{i=1}^{n_{SW}} a_{1,SW,\log \sigma^2,i} \frac{\overline{PC}_{i,SW}}{\sigma(PC_{i,SW})} \right), \quad (\text{A11})$$

Using the same reasoning as for the mean longwave structure (Eq. A5), proportionality coefficient for the longwave logarithmic variance structure ($\lambda_{LW,\log \sigma^2}$) for the PC loadings of the logarithmic variance structure:

$$PC_{i,\Pi \log \sigma_{LW}^2} = \lambda_{LW,\log \sigma^2} \frac{a_{1,LW,\log \sigma^2,i}}{\sigma(PC_{i,LW})} \Rightarrow \lambda_{LW,\log \sigma^2} = \left(\sum_{i=1}^{n_{LW}} \frac{a_{1,LW,\log \sigma^2,i}^2}{\sigma(PC_{i,LW})^2} \right)^{-1/2}. \quad (\text{A12})$$

$$PC_{i,\Pi \log \sigma_{SW}^2} = \lambda_{SW,\log \sigma^2} \frac{a_{1,SW,\log \sigma^2,i}}{\sigma(PC_{i,SW})} \Rightarrow \lambda_{SW,\log \sigma^2} = \left(\sum_{i=1}^{n_{SW}} \frac{a_{1,SW,\log \sigma^2,i}^2}{\sigma(PC_{i,SW})^2} \right)^{-1/2}. \quad (\text{A13})$$

For consistency with the mean structures, we transform the logarithmic variance term (Eq. A8-A9) using Eqs A8, A9, A12, and A13, which yields:

$$c_{LW} \exp \left(\sum_{i=1}^{n_{LW}} \frac{a_{1,LW,\log \sigma^2,i} \times PC_{i,LW}}{\sigma(PC_{i,LW})} \right) = c_{LW} \exp \left(\underbrace{\frac{1}{\lambda_{LW,\log \sigma^2}}}_{d_{LW}} \times \left\langle LW \mid \Pi_{\log \sigma_{LW}^2} \right\rangle_{LW} \right) \quad (\text{A14})$$

$$c_{SW} \exp \left(\sum_{i=1}^{n_{SW}} \frac{a_{1,SW,\log \sigma^2,i} \times PC_{i,SW}}{\sigma(PC_{i,SW})} \right) = c_{SW} \exp \left(\underbrace{\frac{1}{\lambda_{SW,\log \sigma^2}}}_{d_{SW}} \times \left\langle SW \mid \Pi_{\log \sigma_{SW}^2} \right\rangle_{SW} \right) \quad (\text{A15})$$

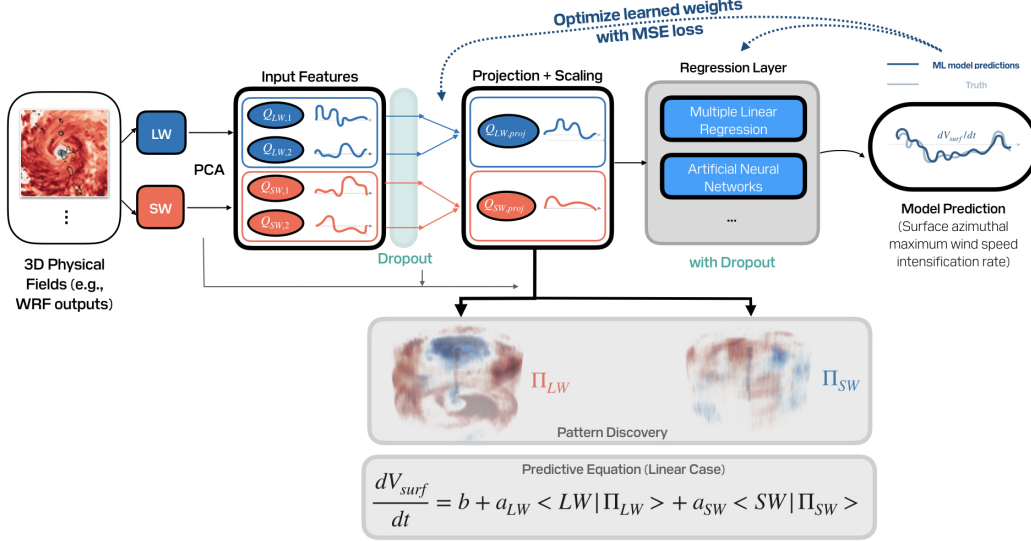


Figure B1. The interpretable linear model baseline to compare to the VED model. This baseline model introduces uncertainty with the dropout operation.

Appendix B Baseline: Principal Component Regression

We implement a simple two-layer linear regression model as a baseline to examine if the more complex VED architecture improves the overall prediction skills and provides a more well-calibrated prediction uncertainty. This baseline is analogous to a two-branch principal component regression (schematic diagram in Fig. B1). The baseline model only extracts two structures from the longwave and shortwave radiation information. These structures are analogous to the μ_{LW} and μ_{SW} in the VED model. Rather than extracting the uncertainty structures and sampling them with the reparameterization trick, we introduce uncertainty in the baseline model using a dropout mechanism. The dropout mechanism zeroes out a random selection of input features, allowing the model to have uncertainties in both the structure layer level and the final prediction outputs. The amount of input features this operation drops is determined by a tunable **dropout rate** hyperparameter that ranges from 0 to 1.

Appendix C Decomposition by Vertical Levels

We isolate the effect of heating anomalies in different vertical levels by zeroing out all grid point values in the input data *except grid points at the interested vertical level*.

Taking longwave radiation as an example, we can separate the LW field into three separate terms:

$$LW = LW_{100} + LW_{1000} + LW_{200-900}, \quad (C1)$$

where LW_{100} (LW_{1000}) is the longwave field where all grid points except those at 100 (1000) hPa are zeroed out, $LW_{200-900}$ is the longwave field where grid points at 100 and 1000 hPa are zeroed out.

Projecting the three components of the right-hand side of Eq. C1 onto the longwave PC eigenvectors yields the same decomposition for the PC loadings:

$$\forall i \in \llbracket 1, n_{LW} \rrbracket, PC_{i,LW} = PC_{i,LW_{100}} + PC_{i,LW_{1000}} + PC_{i,LW_{200-900}} \quad (C2)$$

After standardization, Equation (C2) can be separated into a constant part:

$$\underbrace{\left(\frac{\overline{PC_{i,LW_{100}}} + \overline{PC_{i,LW_{1000}}} + \overline{PC_{i,LW_{200-900}}}}{\sigma(PC_{i,LW})} \right)}_{\overline{PC_{i,LW}}} \quad (C3)$$

and a part that varies in time:

$$\underbrace{\left[\frac{PC_{i,LW_{100}}}{\sigma(PC_{i,LW})} + \frac{PC_{i,LW_{1000}}}{\sigma(PC_{i,LW})} + \frac{PC_{i,LW_{900-200}}}{\sigma(PC_{i,LW})} \right]}_{PC_{i,LW}}, \quad (C4)$$

Substituting Equation C4 into Equation A6 and expanding the first term in Equation A6, we can decompose surface intensification into additive terms that match the long-wave radiative heating field's decomposition of Eq. C1.

$$\begin{aligned} \frac{dV_{surf,24}}{dt} = & \left(\frac{dV_{LW,100hPa}}{dt} + \frac{dV_{LW,200-1000hPa}}{dt} \right) \\ & + \frac{dV_{SW,100-1000hPa}}{dt} + b, \end{aligned} \quad (C5)$$

where $\frac{dV_{LW,100hPa}}{dt}$ quantifies how radiation anomalies at 100 hPa affect the surface intensification.

References

- Akiba, T., Sano, S., Yanase, T., Ohta, T., & Koyama, M. (2019). *Optuna: A next-generation hyperparameter optimization framework*.
- Barnes, E. A., Barnes, R. J., Martin, Z. K., & Rader, J. K. (2022). This looks like that there: Interpretable neural networks for image tasks when location matters. *Artificial Intelligence for the Earth Systems*, 1(3), e220001.
- Behrens, G., Beucler, T., Gentine, P., Iglesias-Suarez, F., Pritchard, M., & Eyring, V. (2022). Non-linear dimensionality reduction with a variational encoder decoder to understand convective processes in climate models. *Journal of Advances in Modeling Earth Systems*, 14(8), e2022MS003130. doi: <https://doi.org/10.1029/2022MS003130>
- Bell, M. M., & Montgomery, M. T. (2019). Mesoscale processes during the genesis of hurricane karl (2010). *J. Atmos. Sci.*, 76(8), 2235-2255. doi: 10.1175/JAS-D-18-0161.1
- Bu, Y. P., Fovell, R. G., & Corbosiero, K. L. (2014). Influence of cloud-radiative forcing on tropical cyclone structure. *J. Atmos. Sci.*, 71(10), 1644-1662. doi: 10.1175/JAS-D-13-0265.1
- Bui, H. H., Smith, R. K., Montgomery, M. T., & Peng, J. (2009). Balanced and unbalanced aspects of tropical cyclone intensification. *Quarterly Journal of the Royal Meteorological Society: A journal of the atmospheric sciences, applied meteorology and physical oceanography*, 135(644), 1715-1731.
- Cangialosi, J. P., Blake, E., DeMaria, M., Penny, A., Latta, A., Rappaport, E., & Tallapragada, V. (2020). Recent progress in tropical cyclone intensity forecasting at the national hurricane center. *WAF*, 35(5), 1913-1922. doi: 10.1175/WAF-D-20-0059.1
- Carstens, J. D., & Wing, A. A. (2020). Tropical cyclogenesis from self-aggregated convection in numerical simulations of rotating radiative-convective equilibrium. *Journal of Advances in Modeling Earth Systems*, 12.

- Carstens, J. D., & Wing, A. A. (2022). A spectrum of convective self-aggregation based on background rotation. *Journal of Advances in Modeling Earth Systems*, 14, e2021MS002860. doi: 10.1029/2021MS002860
- Chen, T.-C., Yau, M.-K., & Kirshbaum, D. J. (2020). Towards the closure of momentum budget analyses in the wrf (v3. 8.1) model. *Geoscientific Model Development*, 13(3), 1737–1761.
- Dai, Y., Torn, M. S., Williams, I. N., & Collins, W. D. (2023). Longwave radiative effects beyond the initial intensification phase of tropical cyclones. *Journal of the Atmospheric Sciences*, 80(7), 1829–1845.
- Delle Monache, L., Eckel, F. A., Rife, D. L., Nagarajan, B., & Searight, K. (2013). Probabilistic weather prediction with an analog ensemble. *Mon. Wea. Rev.*, 141, 3498–3516. doi: 10.1175/MWR-D-12-00281.1
- DeMaria, M., Sampson, C. R., Knaff, J. A., & Musgrave, K. D. (2014). Is tropical cyclone intensity guidance improving? *Bull. Amer. Meteor. Soc.*, 95, 387–398. doi: 10.1175/BAMS-D-12-00240.1
- Eliassen, A. (1952). Slow thermally or frictionally controlled meridional circulations in a circular vortex. *Astrophys. Nor.*, 5, 19–60.
- Emanuel, K. A. (1986). An air–sea interaction theory for tropical cyclones. part i: Steady-state maintenance. *J. Atmos. Sci.*, 43(6), 585–605. doi: https://doi.org/10.1175/1520-0469(1986)043<0585:AASITF>2.0.CO;2
- Fan, Y., Chung, Y. T., & Shi, X. (2021). The essential role of cloud-radiation interaction in nonrotating convective self-aggregation. *Geophys. Res. Lett.*, 48, e2021GL095102. doi: 10.1029/2021GL095102
- Fischer, M. S., Tang, B. H., & Corbosiero, K. L. (2019). A climatological analysis of tropical cyclone rapid intensification in environments of upper-tropospheric trough. *Mon. Wea. Rev.*, 147(10), 3693–3719. doi: 10.1175/MWR-D-19-0013.1
- Gray, W. M., & Jacobson, R. W. J. (1977). Diurnal variation of deep cumulus convection. *J. Atmos. Sci.*, 105, 1171–1188. doi: 10.1175/1520-0493(1977)105<1171:DVODCC>2.0.CO;2
- Haynes, K., Lagerquist, R., McGraw, M., Musgrave, K., & Ebert-Uphoff, I. (2023). Creating and evaluating uncertainty estimates with neural networks for environmental-science applications. *Artif. Intell. Earth Syst.*, 2, 220061. doi: 10.1175/AIES-D-22-0061.1
- Hendricks, E. A., Montgomery, M. T., & Davis, C. A. (2004). The role of “vortical” hot towers in the formation of tropical cyclone diana (1984). *Journal of the atmospheric sciences*, 61(11), 1209–1232.
- Huang, Y.-H., Wu, C.-C., & Montgomery, M. T. (2018). Concentric eyewall formation in typhoon sinlaku (2008). part iii: Horizontal momentum budget analyses. *Journal of the Atmospheric Sciences*, 75(10), 3541–3563.
- Iacono, M. J., Delamere, J. S., Mlawer, E. J., Shephard, M. W., Clough, S. A., & Collins, W. D. (2008). Radiative forcing by long-lived greenhouse gases: Calculations with the aer radiative transfer models. *J. Geophys. Res.*, 113(D13103). doi: 10.1029/2008JD009944
- Ji, D., & Qiao, F. (2023). Does extended sawyer–eliassen equation effectively capture the secondary circulation of a simulated tropical cyclone? *Journal of the Atmospheric Sciences*, 80(3), 871–888.
- Kilroy, G. (2021). Evolution of convective characteristics during tropical cyclogenesis. *Q J R Meteorol Soc.*, 147, 2103–2123. doi: 10.1002/qj.4011
- Kingma, D. P., & Welling, M. (2013). Auto-encoding variational bayes. *arXiv preprint arXiv:1312.6114*.
- Landsea, C. W., & Cangialosi, J. P. (2018). Have we reached the limits of predictability for tropical cyclone track forecasting? *BAMS*, 99(11), 2237–2243. doi: 10.1175/BAMS-D-17-0136.1
- Law, K. T., & Hobgood, J. S. (2007). A statistical model to forecast short-term at-

- lantic hurricane intensity. *Weather and forecasting*, 22(5), 967–980.
- Lipton, Z. C. (2018). The mythos of model interpretability: In machine learning, the concept of interpretability is both important and slippery. *Queue*, 16(3). Retrieved from <https://doi.org/10.1145/3236386.3241340> doi: 10.1145/3236386.3241340
- Mamalakis, A., Barnes, E. A., & Ebert-Uphoff, I. (2023). Carefully choose the baseline: Lessons learned from applying xai attribution methods for regression tasks in geoscience. *Artificial Intelligence for the Earth Systems*, 2(1), e220058.
- Marcinkevičs, R., & Vogt, J. E. (2023). Interpretable and explainable machine learning: A methods-centric overview with concrete examples. *WIREs Data Mining and Knowledge Discovery*, 13(3), e1493. doi: <https://doi.org/10.1002/widm.1493>
- Mayer, K. J., & Barnes, E. A. (2021). Subseasonal forecasts of opportunity identified by an explainable neural network. *Geophysical Research Letters*, 48, e2020GL092092. doi: 10.1029/2020GL092092
- McGovern, A., Lagerquist, R., Gagne, D. J., Jergensen, G. E., Elmore, K. L., Homeyer, C. R., & Smith, T. (2019). Making the black box more transparent: Understanding the physical implications of machine learning. *Bulletin of the American Meteorological Society*, 100(11), 2175–2199.
- Melhauser, C., & Zhang, F. (2014). Diurnal radiation cycle impact on the pregenesis environment of hurricane karl (2010). *J. Atmos. Sci.*, 71(4), 1241–1259. doi: 10.1175/JAS-D-13-0116.1
- Muller, C., & Bony, S. (2015). What favors convective aggregation and why? *Geophys. Res. Lett.*, 42, 5626–5634. doi: 10.1002/2015GL064260
- Muller, C. J., & Romps, D. M. (2018). Acceleration of tropical cyclogenesis by self-aggregation feedbacks. *Proceedings of the National Academy of Sciences*, 115(12), 2930–2935.
- Murthy, V. S., & Boos, W. R. (2018). Role of surface enthalpy fluxes in idealized simulations of tropical depression spinup. *Journal of the Atmospheric Sciences*, 75(6), 1811–1831. doi: 10.1175/JAS-D-17-0119.1
- Nam, C. C., & Bell, M. M. (2021). Multiscale shear impacts during the genesis of hagupit (2008). *Monthly Weather Review*, 149(2), 551–569.
- Narenpitak, P., Bretherton, C. S., & Khairoutdinov, M. F. (2020). The role of multiscale interaction in tropical cyclogenesis and its predictability in near-global aquaplanet cloud-resolving simulations. *Journal of the Atmospheric Sciences*, 77(8), 2847–2863.
- Navarro, E. L., Hakim, G. J., & Willoughby, H. E. (2017). Balanced response of an axisymmetric tropical cyclone to periodic diurnal heating. *Journal of the Atmospheric Sciences*, 74(10), 3325–3337.
- Nicholls, M. E. (2015). An investigation of how radiation may cause accelerated rates of tropical cyclogenesis and diurnal cycles of convective activity. *Atmos. Chem. Phys.*, 15, 9003–9029. doi: 10.5194/acp-15-9003-2015
- Novak, L., & Tailleux, R. (2018). On the local view of atmospheric available potential energy. *Journal of the Atmospheric Sciences*, 75(6), 1891–1907.
- Paszke, A., Gross, S., Massa, F., Lerer, A., Bradbury, J., Chanan, G., ... Chintala, S. (2019). *Pytorch: An imperative style, high-performance deep learning library*.
- Pendergrass, A. G., & Willoughby, H. E. (2009). Diabatically induced secondary flows in tropical cyclones. part i: Quasi-steady forcing. *Mon. Wea. Rev.*, 137, 805–821. doi: 10.1175/2008MWR2657.1
- Ramsay, H. A. (2013). The effects of imposed stratospheric cooling on the maximum intensity of tropical cyclones in axisymmetric radiative-convective equilibrium. *J. Climate*, 26, 9977–9985. doi: 10.1175/JCLI-D-13-00195.1
- Rios-Berrios, R. (2020). Impacts of radiation and cold pools on the intensity and

- vortex tilt of weak tropical cyclones interacting with vertical wind shear. *Journal of the Atmospheric Sciences*, 77(2), 669–689.
- Rogers, R., Reasor, P., & Lorsolo, S. (2013). Airborne doppler observations of the inner-core structural differences between intensifying and steady-state tropical cyclones. *Monthly Weather Review*, 141(9), 2970–2991.
- Rogers, R. F., Reasor, P. D., Zawislak, J. A., & Nguyen, L. T. (2020). Precipitation processes and vortex alignment during the intensification of a weak tropical cyclone in moderate vertical shear. *Monthly Weather Review*, 148(5), 1899–1929.
- Rotunno, R., & Emanuel, K. A. (1987). An air–sea interaction theory for tropical cyclones. part ii: Evolutionary study using a nonhydrostatic axisymmetric numerical model. *J. Atmos. Sci.*, 44(3), 542–561. doi: [https://doi.org/10.1175/1520-0469\(1987\)044<0542:AAITFT>2.0.CO;2](https://doi.org/10.1175/1520-0469(1987)044<0542:AAITFT>2.0.CO;2)
- Ruppert, J. H. (2024, Jan). *ensemble-tropical-cyclone-cases: First official release*. Zenodo. Retrieved from 10.5281/zenodo.10572960 doi: 10.5281/zenodo.10572960
- Ruppert, J. H., & O’Neill, M. E. (2019). Diurnal cloud and circulation changes in simulated tropical cyclones. *Geophys. Res. Lett.*, 46, 502–511. doi: 10.1029/2018GL081302
- Ruppert, J. H., Wing, A. A., Tang, X., & Duran, E. L. (2020). The critical role of cloud infrared radiation feedback in tropical cyclone development. *Proceedings of the National Academy of Sciences*, 117(45), 27884–27892. Retrieved from <https://www.pnas.org/doi/abs/10.1073/pnas.2013584117> doi: 10.1073/pnas.2013584117
- Shimada, U., Aonashi, K., & Miyamoto, Y. (2017). Tropical cyclone intensity change and axisymmetry deduced from gsmf. *Monthly Weather Review*, 145(3), 1003–1017.
- Skamarock, W. (2008). A description of the advanced research wrf version 3. *Tech. Note*, 1–96.
- Smith, W. P., Nicholls, M. E., & R. A. Pielke, S. (2020). The role of radiation in accelerating tropical cyclogenesis in idealized simulations. *J. Atmos. Sci.*, 77(4), 1261–1277. doi: 10.1175/JAS-D-19-0044.1
- Stevens, B., Satoh, M., Auger, L., Biercamp, J., Bretherton, C. S., Chen, X., ... others (2019). Dyamond: the dynamics of the atmospheric general circulation modeled on non-hydrostatic domains. *Progress in Earth and Planetary Science*, 6(1), 1–17.
- Tam, F. I.-H. (2024a, Jan). *Codes for "identifying three-dimensional radiative patterns associated with early tropical cyclone intensification"*. Zenodo. Retrieved from 10.5281/zenodo.10563727 doi: 10.5281/zenodo.10556861
- Tam, F. I.-H. (2024b, Jan). *Trained models and data for "identifying three-dimensional radiative patterns associated with early tropical cyclone intensification"*. Zenodo. Retrieved from <http://dx.doi.org/10.5281/zenodo.10556861> doi: 10.5281/zenodo.10556861
- Tang, B. H. (2017). Coupled dynamic–thermodynamic forcings during tropical cyclogenesis. part ii: Axisymmetric experiments. *J. Atmos. Sci.*, 74(7), 2279–2291. doi: 10.1175/JAS-D-17-0049.1
- Thompson, G., & Eidhammer, T. (2014). A study of aerosol impacts on clouds and precipitation development in a large winter cyclone. *J. Atmos. Sci.*, 71(10), 3636–3658. doi: 10.1175/JAS-D-13-0305.1
- Trabing, B. C., Bell, M. M., & Brown, B. R. (2019). Impacts of radiation and upper-tropospheric temperatures on tropical cyclone structure and intensity. *J. Atmos. Sci.*, 76(1), 135–153. doi: 10.1175/JAS-D-18-0165.1
- Wang, S., Camargo, S. J., Sobel, A. H., & Polvani, L. M. (2014). Impact of the tropopause temperature on the intensity of tropical cyclones: An idealized study using a mesoscale model. *J. Atmos. Sci.*, 71, 4333–4348. doi:

<https://doi.org/10.1175/JAS-D-14-0029.1>

- Wang, Y., Cui, X., Li, X., Zhang, W., & Huang, Y. (2016). Kinetic energy budget during the genesis period of tropical cyclone durian (2001) in the south china sea. *Monthly Weather Review*, 144(8), 2831–2854.
- Wang, Z. (2014). Role of cumulus congestus in tropical cyclone formation in a high-resolution numerical model simulation. *Journal of the atmospheric sciences*, 71, 1681–1700.
- Willoughby, H. E. (1979). Forced secondary circulations in hurricanes. *J. Geophys. Res.*, 84(C6), 3173–3183. doi: 10.1029/JC084iC06p03173
- Wing, A. A. (2022). Acceleration of tropical cyclone development by cloud-radiative feedbacks. *Journal of the Atmospheric Sciences*, 79(9), 2285–2305.
- Wing, A. A., Emanuel, K., Holloway, C., & Muller, C. (2017). Convective self-aggregation in numerical simulations: A review. *Surv Geophys*, 38, 1173–1197. doi: 10.1007/s10712-017-9408-4
- Wing, A. A., & Emanuel, K. A. (2014). Physical mechanisms controlling self-aggregation of convection in idealized numerical modeling simulations. *J. Adv. Model. Earth. Syst.*, 142(6), 59– 74. doi: 10.1002/2013MS000269
- Wu, S.-N., Soden, B. J., & Nolan, D. S. (2021). Examining the role of cloud radiative interactions in tropical cyclone development using satellite measurements and wrf simulations. *Geophys. Res. Lett.*, 48, e2021GL093259. doi: 10.1029/2021GL093259
- Xu, W., Rutledge, S. A., & Zhang, W. (2017). Relationships between total lightning, deep convection, and tropical cyclone intensity change. *Journal of Geophysical Research: Atmospheres*, 122(13), 7047–7063.
- Yang, B., Guo, X., Gu, J.-F., & Nie, J. (2022). Cloud-radiation feedback prevents tropical cyclones from reaching higher intensities. *Geophysical Research Letters*, 49(24), e2022GL100067.
- Yang, B., & Tan, Z. (2018). Interactive radiation accelerates the intensification of the midlevel vortex for tropical cyclogenesis. *Journal of the Atmospheric Sciences*, 77(12), 4051–4065. doi: 10.1175/JAS-D-20-0094.1
- Zagrodnik, J. P., & Jiang, H. (2014). Rainfall, convection, and latent heating distributions in rapidly intensifying tropical cyclones. *Journal of the Atmospheric Sciences*, 71(8), 2789–2809.
- Zhang, F., & Emanuel, K. (2016). On the role of surface fluxes and wishe in tropical cyclone intensification. *Journal of the Atmospheric Sciences*, 73(5), 2011–2019. doi: 10.1175/JAS-D-16-0011.1